

NOWCASTING PRECIPITATION ONSET IN VANCOUVER USING
CORALNet-UBC LIDAR IMAGERY

by

ANNIE F. SEAGRAM

A THESIS SUBMITTED IN PARTIAL FULFILLMENT OF
THE REQUIREMENTS FOR THE DEGREE OF

BACHELOR OF SCIENCE (HONOURS)

in

THE FACULTY OF SCIENCE

(Environmental Sciences)

This thesis conforms to the required standard

.....
Supervisor

THE UNIVERSITY OF BRITISH COLUMBIA
(Vancouver)

APRIL 2010

© Annie F. Seagram, 2010

ABSTRACT

In recent years, the application of ground-based LIDAR (LIght Detection And Ranging) to atmospheric observation and monitoring has become increasingly common. The UBC (University of British Columbia) CORALNet (Canadian Observational Research Aerosol Lidar Network) lidar dataset exhibits an interesting cloud signature on numerous daily plots from the 1064/532 nm lidar imagery. The signature features a general downward sloping of cloud cover over time, ending in a precipitation event (marked by lidar shutoff by rain sensor). These Cloud Lowering Signatures (CLOSs) are unique in their shape, slope, and rate of decline (from first appearance to onset of precipitation). The focus of this study was to explore the real-time use of lidar imagery for nowcasting, by deriving a conceptual model based on CLOS characteristics. A synoptic map-typing procedure using sea-level pressure maps was applied to each of the 75 CLOSs catalogued from April, 2008, to September, 2009. Eight map classes were derived, most of which were associated with low pressure conditions. Additional temporal parameters from the lidar imagery were collected to produce statistically significant empirical models for each map class in order to predict the lead time to precipitation onset based on a linear rate of lowering of the cloud cover. In real time, the models accurately predicted the onset of precipitation, between 0.23 – 4.57 hrs of the actual lead time. However, these results were only preliminary due to the small dataset examined ($n = 7$). It is hoped that the results of this study may be used to nowcast precipitation onset with greater accuracy, and to serve as a precursor to automated methods that may exploit quantitative data as forecasting products.

TABLE OF CONTENTS

TITLE PAGE	i
ABSTRACT	ii
TABLE OF CONTENTS	iii
LIST OF FIGURES	v
LIST OF TABLES	vi
LIST OF PLATES	vii
LIST OF DIGITAL MEDIA	vii
LIST OF ACRONYMS	viii
ACKNOWLEDGEMENTS	ix
1.0 INTRODUCTION	1
1.1 Previous work using lidars.....	2
1.1.1 Cloud-base height.....	3
1.1.2 Atmospheric boundary layer structures.....	4
1.1.3 Frontal passage	4
1.1.4 Other atmospheric phenomena	4
1.2 Phenomenological Conceptual Models.....	5
1.3 Objectives.....	5
2.0 BACKGROUND	
2.1 Geography and meteorology of Vancouver.....	6
2.2 Meteorological seasonal and diurnal variations	7
3.0 METHODS	
3.1 Overview.....	8
3.2 Data sources.....	8
3.2.1 Cloud Lowering Signatures (CLOSs)	8
3.2.2 Maps and satellite images	12
3.2.3 Meteorological data	13
4.0 MANUAL SYNOPTIC MAP CLASSIFICATION AND CLIMATOLOGY OF CLOSs	
4.1 Underlying assumptions	13
4.2 Procedure description	14

4.3 Synoptic classification and characteristics of CLOSs.....	18
5.0 CLOS LIDAR PARAMETERS	
5.1 Methods and analysis	21
5.2 Synthesis	26
5.3 Relations between CLOS lidar parameters and other meteorological data	27
6.0 SUBJECTIVE PREDICTORS	28
6.1 Class C.....	28
6.2 Class F	31
6.3 Problematic shape-types.....	33
7.0 DECISION TREE IMPLEMENTATION: “A USER’S GUIDE”	34
8.0 NOWCASTING PRECIPITATION ONSET: MODEL VALIDATION	
8.1 Introduction	40
8.2 Approach to validation	40
8.3 Validation results	41
8.4 Assessment.....	47
8.5 Future work and usage.....	48
9.0 CONCLUSION	49
REFERENCES CITED	50

LIST OF FIGURES

Figure 1. Map of Vancouver and surrounding region.....	2
Figure 2. Example of a CLOS, observed by the CORALNet-UBC lidar from May 9 th 14:25 to May 10 th 00:40 (PDT), 2008.	3
Figure 3. Schematic diagram of general methodology.....	9
Figure 4. CORALNet-UBC lidar in a modified cargo trailer, located on UBC campus, Vancouver.....	9
Figure 5. Interpretation for extracting CLOS data from lidar imagery.....	11
Figure 6. Distribution of low pressure system centers for Class A and B.....	15
Figure 7. Schematic diagrams of synoptic map-type classes.....	17
Figure 8. Distribution of CLOS cases that ended in precipitation for each synoptic map-type class.....	19
Figure 9. Distribution of shape types by class.....	20
Figure 10. Seasonal distribution of cases for each class.....	21
Figure 11. Plots for rate of lowering and lead time of CLOSs by class.....	23
Figure 12. Plots for cloud-base starting altitude versus total lowering for each CLOS, by synoptic map class.....	25
Figure 13. Windrose for all low pressure classes (Class A – E).....	27
Figure 14. Plot of Rate of Lowering (m/h) versus lead time (h) for all synoptic map-type classes.	29
Figure 15. Decision tree for nowcasting precipitation onset.	36- 39
Figure 16. A hypothetical CLOS and methods used to nowcast precipitation onset.....	41
Figure 17. Resultant CLOSs from lidar imagery (left) and corresponding SLP/IR composite (right) maps used for model validation.....	42 – 44
Figure 18. Nowcasting results for precipitation onset using the decision tree.....	45

LIST OF TABLES

Table 1. Shape-types for CLOSs based on cloud-base lowering	12
Table 2. Summary of map class distribution.	18
Table 3. Nonlinear regression results for lead time response to RL	24
Table 4. Linear regression results for total lowering response to initial cloud-base height....	26
Table 5. Hypothetical model predictions for CLOS lead time based on an initial input RL of 400 m/h	26
Table 6. Subjectively determined features of all Class C cases which may or may not lead to precipitation onset.....	30
Table 7. Results of the ANOVA for starting cloud-base heights partitioned by onset of precipitation or lack thereof	31
Table 8. Detailed features of all Class F cases which may or may not lead to precipitation onset.	32
Table 9. Summary of nowcasting results using the derived model.	45

LIST OF PLATES

PLATE A: CATALOGUE OF CLOUD LOWERING SIGNATURES..... *back page*

LIST OF DIGITAL MEDIA

CONTENTS.....DVD, *CONTENTS.txt*
CLASSES..... DVD, *folder*
ANALYSIS SHEETS..... DVD, *folder*
CORALNet-UBC LIDAR IMAGERY..... DVD *folder*

LIST OF ACRONYMNS

CORALNet	Canadian Operational Research Aerosol Lidar Network
UBC	University of British Columbia (Vancouver)
LIDAR (lidar)	Llght Detection And Ranging
CLOS	Cloud LOvering Signature
CYVR	refers to: Vancouver International Airport weather station
SLP	Sea Level Pressure
IR	Infrared
USA	United States of America
BC	British Columbia
WA	Washington State, USA
RL	Rate of lowering
ANOVA	ANalysis Of VAriance
METAR	MEteorological Terminal Aviation Routine weather Report
DT	Decision Tree

ACKNOWLEDGEMENTS

I would like to take this opportunity to extend my most sincere gratitude to those who helped make this work possible. First and foremost, to my supervisor, Dr. Ian McKendry, thank you for your support, commitment, patience and understanding throughout the entire process. Without the weekly meetings and your constant enthusiasm, none of this study would have been possible. Thank you for keeping me on track when it was most needed, and inspiring me to keep persevering and learning. I would also like to acknowledge the contributions by Dr. Kevin Strawbridge, who initially set up the CORALNet-UBC lidar site and suggested the research topic presented here.

Thanks to the honours advisors, Dr. Douw Steyn, Dr. Tara Ivanochko, and Dr. Mary Lou Bevier, whose support and encouragement were always appreciated. To Douw, thank you for the additional comments and criticism, and endless discussions that helped me through this process. Your guidance over the past year and half has been invaluable.

My sincere gratitude to Dr. Roland Stull and his research team members, May Wong and Thomas Nipen, for giving me access to the Environment Canada archives and effectively working their schedules around mine. It is truly appreciated. Thank you to Neal Johnson and the University of Wyoming Department of Atmospheric Science for providing decoded meteorological datasets. Also, many thanks to Rich Pawlowicz for providing useful MATLAB codes and answering my many questions. Thanks for the contributions provided by Adrian Jones, Christopher Seagram, Leah Adam, Justin Lau, and the UBC Department of Earth and Ocean Sciences.

Finally, the support from my family and peers has been remarkable. Thanks to those who believed that I really could manually handle and analyse 75 individual maps; and thanks to those who didn't, for the extra motivation.

1.0 INTRODUCTION

In recent years, the application of ground-based LIDAR (LIght Detection And Ranging) to atmospheric observation and monitoring has become increasingly common. Lidars are unique in that they provide continuous, high resolution time/height representations of both natural and anthropogenic atmospheric particulates (aerosols). When processed, the lidar output can facilitate a multitude of different studies, dealing with both the temporal/spatial structure and evolution of atmospheric phenomena, and aerosol characteristics (e.g. McKendry *et al.* 2009, Yumimoto *et al.* 2007, Melfi *et al.* 1989). Lidars are often implemented with a suite of other active and passive sensors (e.g. satellite imagery, Doppler radar, microwave radiometer; e.g. Illingworth *et al.* 2007) to bridge observational gaps in data for rapidly changing meteorological phenomena.

The first observation site of the Canadian Observational Research Aerosol Lidar Network (CORALNet) was established on the University of British Columbia (UBC) campus, Vancouver (Figure 1), to study long-range transport of aerosols and monitor air quality. Vancouver (49.281°N, 123.141°W) was chosen as a site of interest as there are few measurements of aerosols along the west coast of North America (CORALNet 2010). The dual-wavelength 1064/532 nm lidar began collecting data on April 16th, 2008. All first-look images of the output are publicly available on the website (www.coralnet.ca).

Of significance in this study is an interesting cloud signature, observable on numerous daily plots of the CORALNet-UBC dataset. The signature features a general downward sloping of cloud cover over time, ending in a precipitation event (marked by lidar shutoff via rain sensor; Figure 2). These Cloud LOWering Signatures (CLOSs) are unique in their shape, slope, and rate of decline (from first appearance to onset of precipitation). The focus of this study is to determine (1) the synoptic-scale weather feature(s) that results in these events; (2) the observed weather conditions which may contribute to the characteristic shape and/or rate of lowering of the cloud cover, and (3) how the real-time lidar output, in combination with

(1) and (2), can be used to nowcast (short-term weather forecast) precipitation events with greater accuracy. Intended is that the results may be used as a precursor to analytical studies that may exploit quantitative data as forecasting products for data assimilation in forecast models, and that a conceptual model may be used to provide forecast guidance.



Figure 1. Map of Vancouver and surrounding region. The CORALNet-UBC lidar is located at point A, on UBC campus. B is the location of the CYVR weather station. The inset map shows Vancouver's location on the west coast of British Columbia at point C. Data used in this study was also taken from Quillayute, Washington, at point D. Figure modified from Google Earth (2010), inset map created using MATLAB codes by R. Pawlowicz (2009).

1.1 Previous work using lidars

The following sections are a summary of various lidar-based studies. The focus of the subsequent literature review is on ground-based, vertical-pointing (elastic backscattering) lidars, especially in connection with precipitation and cloud structures.

Backscatter Ratio at 1064 nm from 2008/05/09 14:25:00 to 2008/05/10 14:25:00

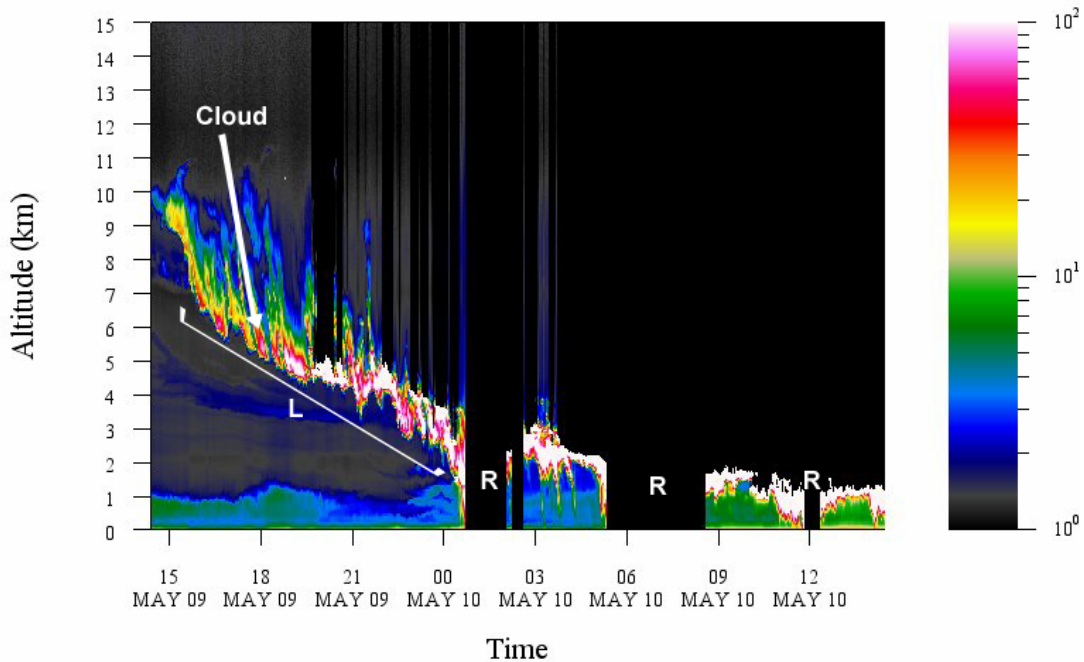


Figure 2. Example of a CLOS, observed by the CORALNet-UBC lidar from May 9th 14:25 to May 10th 00:40 (PDT), 2008. The lowering of cloud-base is marked by L. Note the multiple bands of precipitation marked by lidar shutoff at points R, and a distinct concave-upwards lowering of cloud-base. Modified from CORALNet (2010).

1.1.1 Cloud-base height

Cloud-base height is the most reliable information derived from ground-based lidars (Melfi *et al.* 1989), and is more common than the detection of cloud-top heights due to the attenuation of the lidar signal before the cloud-top is reached (Pal *et al.* 1992). The measurement of cloud-base height and vertical cloud distribution often involves the application of an automated algorithm for detection (e.g. Pal *et al.* 1992, Wang & Sassen 2001), where identifying clear regions through the troposphere is possible (Morille *et al.* 2007). Cloud-base height detection can be complementary to satellite measurements of the same cloud system in deriving meaningful information of cloud coverage and vertical

distribution (Pal *et al.* 1992). In these instances, lidar measurements can be used to identify low-level water clouds that are indistinguishable by radar (Illingworth *et al.* 2007).

1.1.2 Atmospheric boundary layer structures

Several different techniques to determine the boundary layer (BL) heights from lidar systems have been implemented (e.g. Brooks 2003, Morille *et al.* 2007, McKendry *et al.* 2009). Lidars have the ability to measure properties of the BL that are otherwise unobtainable within a desired spatial-temporal scale (Brooks 2003). Additionally, under convective conditions, the mixed layer (ML) depth may be measured by means of automated extraction schemes on lidar output to develop objective, robust measurements (Steyn *et al.* 1999).

1.1.3 Frontal passage

Clouds are easily identifiable on lidar imagery, corresponding to regions of maximum backscattering. The continuous temporal coverage of lidars through large depths of the vertical atmosphere implies that details of frontal passage (such as slope, frontal zone thickness, and turbulent mixing) are interpretable (Melfi *et al.* 1989). Levels of backscattering ratios correspond to the aerosol concentration and composition associated with different air masses during frontal passages. Particularly, cold fronts are characterised by sharply decreasing backscattering at lower altitudes (Sakai *et al.* 2005). Lidar imagery is also advantageous when observing the spatial and temporal structural evolution of convective storms, especially those that produce extreme rainfall rates over complex topography (Zhang *et al.* 2009)

1.1.4 Other atmospheric phenomena

Lidars are able to detect a multitude of transient atmospheric events. These include, but are not limited to, forest fire plumes (e.g. McKendry *et al.* 2009), firework plumes (van der Kamp *et al.* 2008), medium- to low-frequency gravity waves (Rauthe *et al.* 2008), and when using lidar network to track spatial distribution, aerosol and pollution advection

(McKendry *et al.* 2009) and dust transport over large spatial scales (e.g. Yumimoto *et al.* 2007, Murayama *et al.* 2001).

1.2 Phenomenological Conceptual Models

The difficulties facing forecasters in the Pacific Northwest are much the same that any forecaster must overcome, such as: horizontal and vertical resolutions, input of boundary conditions, initial conditions, the simplified relationships between variables (primitive equations), and parameterization. However, the locality of Vancouver on the western coast of Canada and the windward side of the Coast Mountains poses additional problems to forecasters and modelers. Various processes that occur on smaller scales than model resolution (e.g. thermally forced circulations, mountain/valley breezes), complex terrain and topography, the lack of observational data from the Pacific Ocean (known as the “Pacific Data Void”) to input initial conditions, and sparse radar coverage due to topography are all problems that forecasters must deal with in some manner (Colman 2003).

A phenomenological conceptual model may be implemented to maximize the forecaster’s perception of physical processes, and to minimize incorrect judgment (Colman 2003). These models are also immediately useful in nowcasting, as they delineate and select sensitive predictors that are not necessarily resolved at the scale of the numerical model (Colman 2003). Thus, conceptual models are imperative for human forecasters, and subjectivity should not be discredited. Conceptual models in meteorology often manifest as decision trees, such as those used by Colquhoun (1987) to forecast thunderstorms, or by the National Weather Service Seattle Forecast Office to forecast Enumclaw winds (Colman 2003).

1.3 Objectives

From the literature, it is evident that lidars are primarily used in a passive, observational manner in order to verify and measure atmospheric structures and phenomena. By using continuous lidar output and exploiting cloud signatures in real-time to nowcast precipitation onset, lidar observations could be established as a tool for public advisories. The

overall objective here was to develop and test a simple model to utilize real-time lidar imagery to forecast the timing of precipitation based on evolving cloud signatures.

This paper is a two-phase study of the CLOSs as revealed by CORALNet-UBC lidar imagery. The first chapters present the background literature and information that lead to the development of the present research. Chapter 3 presents the general methodology and data sources used in the analysis. Chapter 4 is the first phase of the study, in which the cloud signatures are interpreted and analysed by means of a manual map-typing procedure to develop the first steps of a conceptual model (decision tree). In Chapters 5 and 6, quantitative and subjective analyses are done to produce a prediction model for precipitation onset, which is summarized in Chapter 7. The results are actively implemented and discussed in Chapter 8.

2.0 BACKGROUND

2.1 Geography and meteorology of Vancouver

Vancouver is a densely populated coastal metropolitan city, with a population of over two million. It is located in the western sector of the triangular-shaped Lower Fraser Valley, with the Fraser River bordering its southern edge and the Strait of Georgia to the west. The North Shore Mountains are located northeast of the city, oriented northwest to southeast.

The climatology of Vancouver is explained by its mid-latitude location on the west coast of Canada, topography, proximity to the Pacific Ocean, and urban development. The city is known for its cool season rainfall. Vancouver is located on the storm track of the North Pacific latitude low-pressure systems (Oke & Hay 1994; Barry & Carleton 2001). These systems may last for three to five days, but are usually late in their life cycle once they reach Vancouver, and can die out (cyclolysis) in the Gulf of Alaska just northwest of B.C. in the “cyclone graveyard” (Stull 2009). Local climate variations are evident, with near-shore locations experiencing the effects of land-sea contrasts (Oke & Hay 1994).

As expected, the distribution of precipitation is governed by the topography. The mountains influence the approaching airmasses well upwind. For every 100 m increase in elevation, there is a corresponding 100 mm increase in precipitation (Oke & Hay 1994).

Winds in the Vancouver region are strongly influenced by channeling via topography and thermally-induced circulations, i.e. sea/land breezes and mountain/valley winds (Oke & Hay). These controls result in a predominant easterly wind, as indicated in the 30-year climate normals for CYVR (Vancouver International Airport weather station) (Environment Canada 2010).

2.2 Meteorological seasonal and diurnal variations

Maximum rainfall occurs in the winter, when low pressure disturbances are common. Specifically, the precipitation maximum occurs in the winter (November-December-January) period (Environment Canada 2010). Snow accumulation is not as common as rainfall, but tends to peak in the month of January. In spring, summer and fall, convective storms also develop (Oke & Hay 1994). Wintertime precipitation is on the order of three to four times greater than summer totals. These winter months are characterized by widespread cloud cover, peaking at an average of 552 hrs with 8 – 10 tenths of cloud coverage for the month of January (Environment Canada 2010). January precipitation occurs most frequently at night and less frequently in the afternoon, whereas July precipitation is more frequent in the early afternoon, and less frequent in the evening (Oke & Hay 1994).

3.0 METHODS

3.1 Overview

In this chapter, a methodological overview used to develop a nowcasting model for precipitation onset in Vancouver using lidar imagery is described. The general development of the model based on CLOSs from lidar imagery can be summarized in five steps:

1. Create a catalogue of CLOSs and collect temporal and spatial data from their corresponding lidar images
2. Produce a synoptic map classification scheme to classify the synoptic conditions associated with each CLOS
3. Analyse the meteorological data corresponding to each CLOS to create a conceptual model
4. Re-analyse any problematic cases to provide any additional subjective predictors, and
5. Test the models in real-time to nowcast precipitation and validate their predictive ability

A schematic flowchart of these steps is shown in Figure 3 below. Through these steps, between-group variability of sea-level pressure (SLP) maps was generated, followed by within-group analyses. The methods undertaken were tailored as needed as results from the preceding steps were made available.

3.2 Data sources

3.2.1 *Cloud Lowering Signatures (CLOSs)*

Numerous data sources were collected in the development of the conceptual model for nowcasting precipitation onset. Firstly, a catalogue of CLOS cases was generated based on the CORALNet-UBC daily first-look images of lidar imagery. The lidar is remotely controlled and located in a modified cargo trailer (Figure 4) on UBC campus (Figure 1) (CORALNet 2010). The laser simultaneously emits two wavelengths (1064 and 532 nm) at

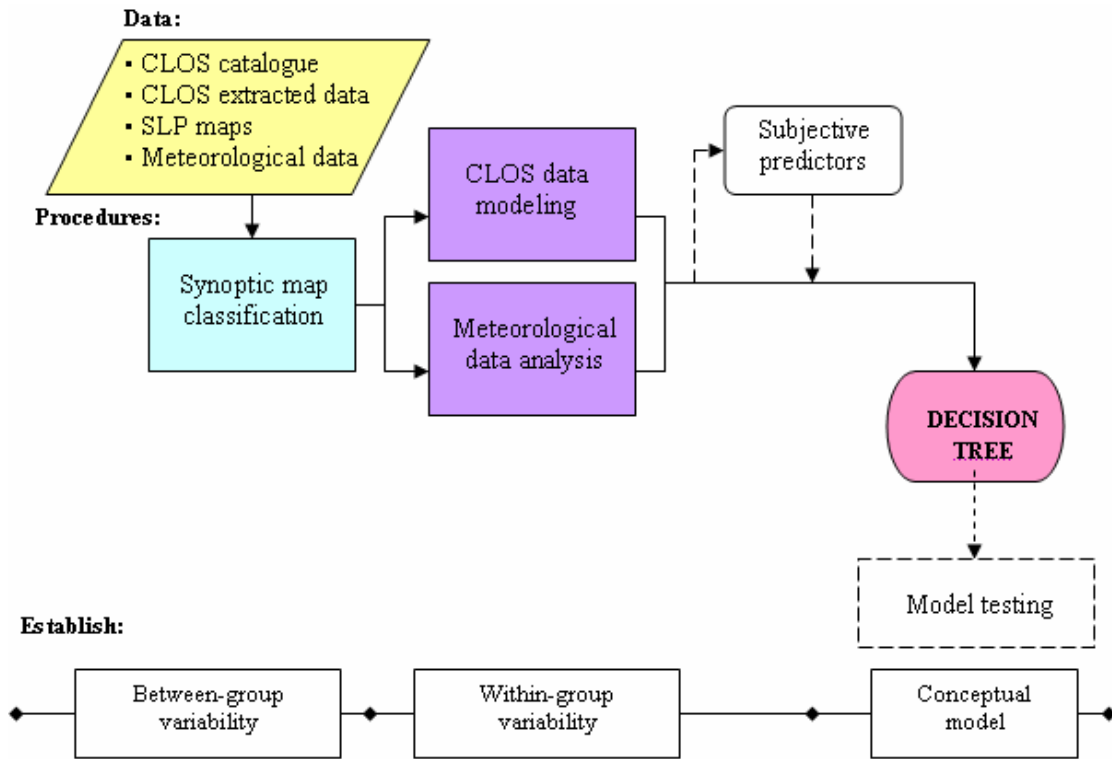


Figure 3. Schematic diagram of general methodology



Figure 4. CORALNet-UBC lidar in a modified cargo trailer, located on UBC campus, Vancouver. The red arrow points to the roof hatch that closes at the onset of precipitation, causing the lidar to effectively shut off. Modified from CORALNet (2010).

10 Hz, and measures a return backscattering signal at 3 channels (532 nm polarization) from the surface to 15 km. The trailer is also equipped with a meteorological tower and precipitation sensor that closes the roof hatch at the onset of precipitation. There may be significant down time of lidar operation due to maintenance, aircraft passages overhead, and reactivation sequences following precipitation events. For the purpose of this study, the 1064 nm daily plots were analysed for cloud signatures. Due to several cases of erroneous or missing data, meteorological data from the lidar station itself was not used in subsequent analyses (see section 3.1.3).

CLOS cases were numbered sequentially, from April 16th, 2008, to September 1st, 2009. This time period was chosen based on the availability of data, and to best capture synoptic meteorological variability and seasonal changes. Each case was defined by the apparent start of cloud lowering to the end of lowering. By this definition, not each case was associated with precipitation, as several lowering events did not end in lidar shutoff. For the CLOSs that did end in precipitation, the time of significant precipitation onset was recorded, and brief periods of intermittent precipitation (approximately <1 hr) were ignored. Whether the CLOS resulted in precipitation or not was also noted in the main catalogue (Plate A).

The starting and ending cloud-base heights corresponding to the start and end time, respectively, were recorded. The ending cloud-base height was assumed to be the highest delineation of backscattering before lidar shutoff, as large ‘swaths’ of backscattering (most likely virga) were common at lower altitudes before precipitation onset. For the purpose of visually comparing the cases, each CLOS was replotted into 24-hour windows. The season of occurrence was also recorded, defined as winter (December-January-February), spring (March-April-May), summer (June-July-August), and fall (September-October-November). A summary of the data extract from the lidar imagery is presented in Figure 5.

Each CLOS was then designated a shape-type, corresponding to its general shape of lowering of the cloud-base. Six general shape types were observed: linear (L), more than one linear feature (M), re-lowering (R) concave upwards (C), concave downwards (D), and S-shaped (S). Details are outlined in Table 1.

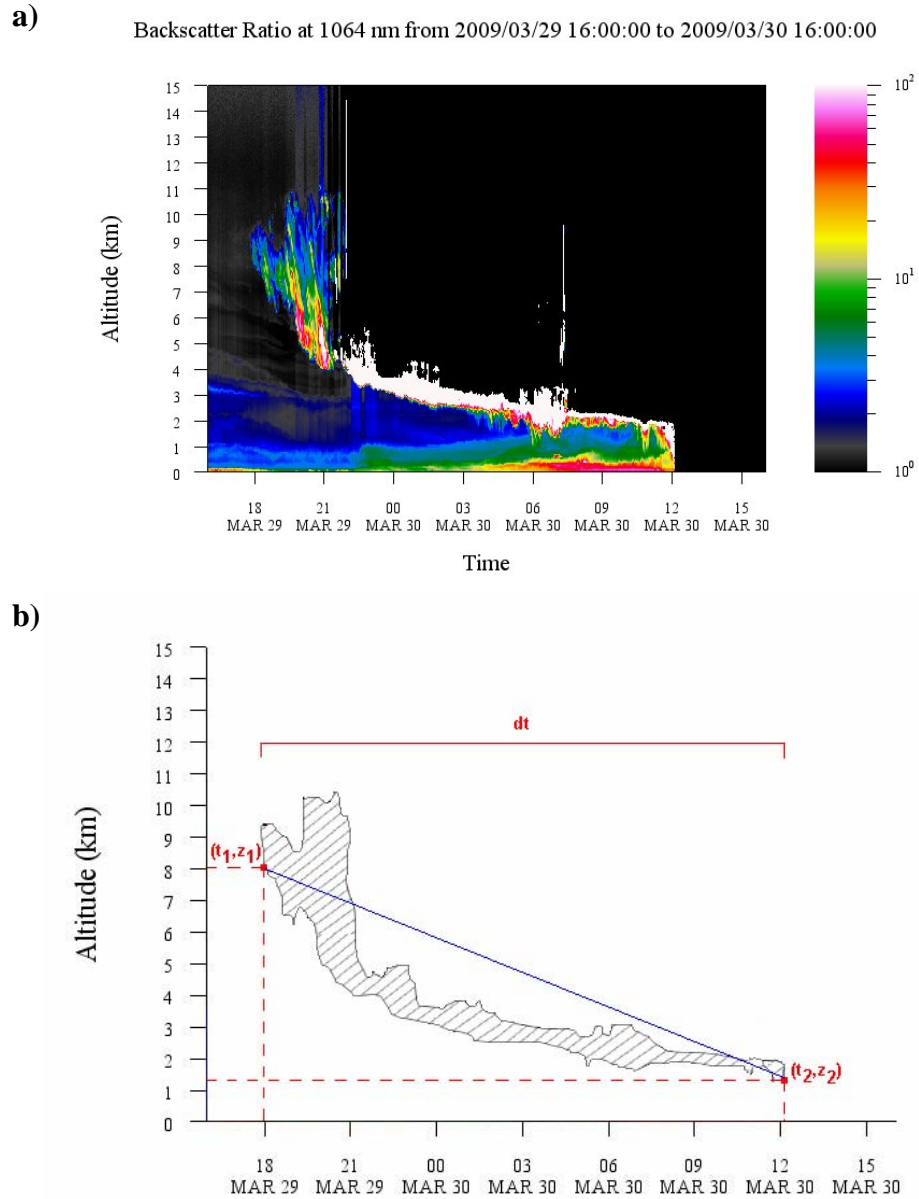


Figure 5. Interpretation for extracting CLOS data from lidar imagery. (a) is the actual lidar output, and (b) is the interpreted and interpolated data used in subsequent analyses. In (b) cloud cover is represented by the hatched region; t_1 and t_2 are the start and end times of the CLOS, respectively; z_1 and z_2 are the start and end cloud-base heights (m), respectively; dt is the lead time to precipitation onset. The blue line represents the calculated linear rate of lowering (RL) of cloud cover. Figure (a) obtained from CORALNet (2010).

Table 1. Shape-types for CLOSs based on cloud-base lowering

Code	Shape	Description	Schematic cloud- base
L	Linear	Clear linear slope of cloud base	
M	More than one linear feature	Clear linear slope of cloud base. An additional linear sloping is apparent overlapping aloft. (The signal of the first lowering is not attenuated completely). Slopes are not necessarily parallel to each other.	
R	Re-lowering	Clear linear slope of cloud base. The initial slope end, and a new slope begins aloft. The two linear slopes are associated with one synoptic system. Slopes are not necessarily parallel to each other.	
C	Concave upwards	Exponential decrease of cloud base with gradually decreasing slope. Cloud base may become parallel to ground near end time.	
D	Concave downwards	Initial slope of cloud base is lowering gradually, then rapidly increases.	
S	S-shape	Sideways S-shape; produces a tiered lowering. Multiple tiers are possible.	

3.2.2 Maps and satellite images

Surface plot maps of sea-level pressure (SLP) and infrared (IR) satellite imagery were obtained from the Environment Canada online archive server. SLP maps extended from approximately 45° to 65° N, and from 105° to 175° W. Maps and images corresponded to the time sequence of each CLOS. SLP maps were available every 6 hrs, and IR satellite imagery every 2 hrs. Each was taken to the nearest hour of the CLOS start to end time. The continuous time sequence of SLP maps for each CLOS provided additional guidance for subsequent classification of ambiguous cases.

3.2.3 Meteorological data

Station data from CYVR (Vancouver International Airport weather station) was obtained via Unidata (Unidata Program 2009). All basic meteorological data (METARs) was available every hour, including: SLP, temperature, dew point temperature, surface wind speed and direction, cloud cover, cloud ceiling, cloud type, and visibility. Pressure tendency was available every 6 hrs. Upper air data at the 500 mb level was obtained from the University of Wyoming Department of Atmospheric Science, available every 12 hrs. The 500 mb level was chosen as it is usually considered the “steering level” for mid-latitude cyclones. 500 mb wind speed and direction was obtained from the Quillayute (KUIL, Washington, USA; Figure 1) station, as it was the closest station to Vancouver with available data.

4.0 MANUAL SYNOPTIC MAP CLASSIFICATION AND CLIMATOLOGY OF CLOSs

In this section, a manual synoptic climatology of CLOSs is developed based on the circulation-to-environment approach of Yarnal (1992), whereby the general synoptic conditions of the atmosphere (pressure fields) are used to qualify the resulting environmental conditions (CLOSs and precipitation onset). After establishing the basic assumptions of the approach, the derived map classifications are described alongside their dominant synoptic conditions relating to the CLOSs.

4.1 Underlying assumptions

Manual map typing procedures involve several initial assumptions. Firstly, using a circulation-to-environment classification assumes that the atmospheric circulation determines the surface environment (Yarnal 1992). In this case, it is assumed that the SLP map corresponds to the cloud signature as depicted in the lidar imagery, and that the temporal

scale of the SLP map and beginning of the lidar CLOS sufficiently match each other. Map typing procedures also imply that atmospheric circulation can be “partitioned into discrete, non-overlapping intervals” (Yarnal 1992, p. 11). That is, synoptic conditions are independent from one another. In reality, this may not be true due to up-wave and down-wave influences, yet it is a necessary assumption to separate synoptic maps. In saying this, all data associated with the CLOSs were treated as *independent* in statistical analyses. We must also consider that the map typing procedure did indeed capture all possible synoptic conditions, while maximizing between-group variance and minimizing within-group variance of the synoptic types.

4.2 Procedure description

Pressure fields revealed by SLP maps over the northeast Pacific Ocean were used to determine the between-group variability of the CLOSs. The IR satellite imagery was used as additional guidance when interpreting unclear SLP maps, as they covered a larger area of the Pacific and thus more synoptic features (particularly cloud cover) were distinguishable. After identifying each CLOS, the SLP map corresponding to the start time of lowering was selected for classification. A static classification was appropriate, since the synoptic conditions at the instant of CLOS onset was used as a predictor for cloud signature development (the compiled analysis sheets used for manual classification can be found on the digital media DVD provided).

Initially, the maps were classified into either predominantly low or high pressure fields. General pressure features, including location and pressure gradient strength, were then used to generate eight map classes. This process was repeated several times to ensure consistency. All classes were generated independent of any CLOS features or seasonality.

The maps which did not meet any of the grouping criteria were deemed “unclassifiable”. As well, signatures that were initially catalogued but later appeared to be too sporadic, sparse, or with weak backscattering were removed. Some consideration was given to maps with low pressure systems “out of the frame” of the SLP map, but apparent on the IR imagery, or which had multiple features to consider. For example, cases with an SLP

map revealing several dispersed lows dominating the Pacific and coastline were “tracked” through the duration of the CLOS to decide which feature was most influential on the Vancouver region. The following summarizes each of the eight synoptic map classes:

Class A: a single, well-developed low pressure system is present over the northeast Pacific. A high pressure ridge is located either over the northwest portion of the USA (Washington) and/or southern BC, or offset westward from the coast. The highest pressure of the ridge is located south of the low pressure center. The low pressure center is located at a mean longitude of 150.3°W , and mean latitude of 55.0°N , with a standard distance of 4.8° (Figure 6).

Class B: similar to Class A, a single, well-developed low pressure system is present over the northeast Pacific, with a high pressure ridge over northwestern USA, southern BC or offset westward from the coast. Unlike Class A, the highest pressure of the ridge is located along the same latitude or north of the low pressure center. The low pressure center is located at a mean longitude of 143.7°W , and mean latitude of 49.6°N , with a standard distance of 5.6° (Figure 6). Thus, Class B tends to be located further south than systems associated with Class A.

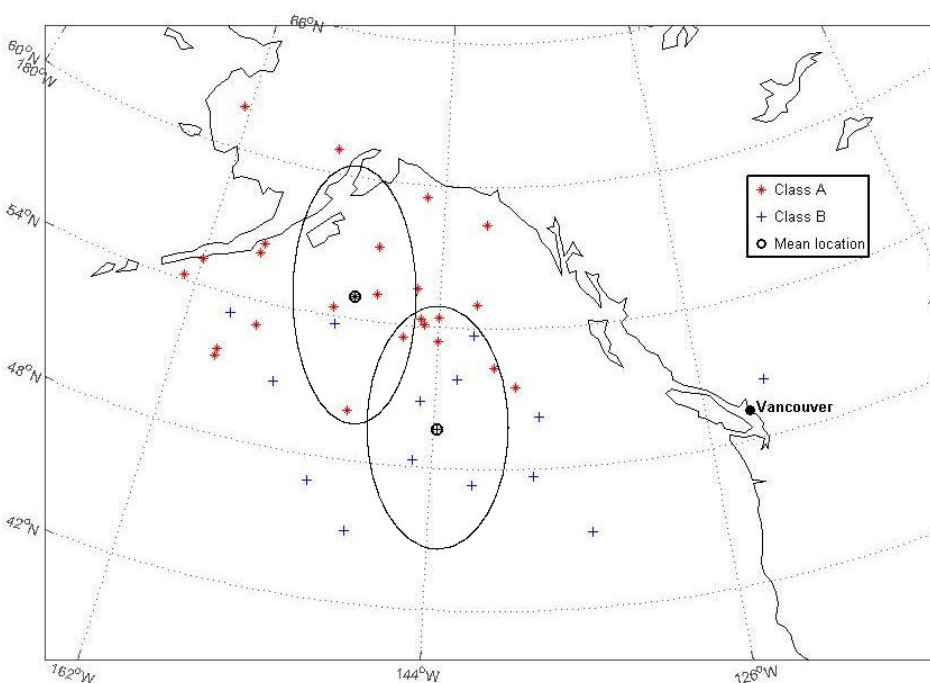


Figure 6.

Distribution of low pressure system centers for Class A and B. Included is a circle delineating the standard distance of the mean location of the low center for each class. Uses MATLAB codes by R. Pawlowicz (2009).

Class C: low pressure areas (either well-developed systems or relative cut-off regions of low pressure) are present in the western portion of the Gulf of Alaska as well as over the northwest portion of the USA and/or western Canada. High pressure regions are located over Alaska and/or northeast Canada, as well as over the Pacific offshore and southwest of Canada. The two areas of high pressure may either be well-developed (tight isobars) or relatively ‘blended’ together. When well-developed, the overall appearance of the isobars gives rise to a col (‘saddle point’) over the Pacific or near the coastline.

Class D: more than one well-developed low pressure system is present over the Pacific. The systems are concentric (seemingly ‘joined’) or close together. A high pressure ridge is present over northwestern USA and/or southern BC.

Class E: more than one well-developed low pressure system is present over the Pacific. The systems are not concentric and are distinctly cut-off from each other. A high pressure ridge is present over northwestern USA and/or southern BC.

Class F: a large-scale high pressure system dominates the Pacific. Lows are not present, or are weakly developed or isolated.

Class G: a large-scale high pressure system is present over the entire western coast of Canada, and may intrude into northern USA. Isobars are approximately parallel to the coastline of western Canada, sloping from northwest to southeast. A low pressure system may be present far from shore in the southwestern portion of the Gulf of Alaska.

Class H: a broad low pressure trough is present to the west, stretching southward longitudinally from northwestern Alaska. This system is lead by a smaller (short-wave) low pressure system. A broad high pressure system is present over the west coast.

A schematic diagram of each class is shown in Figure 7. Note that Classes A through E are associated with dominant low pressure systems over the Pacific and/or Gulf of Alaska, Class F is associated with high pressure, and Classes G and H do not distinctly fit either group.

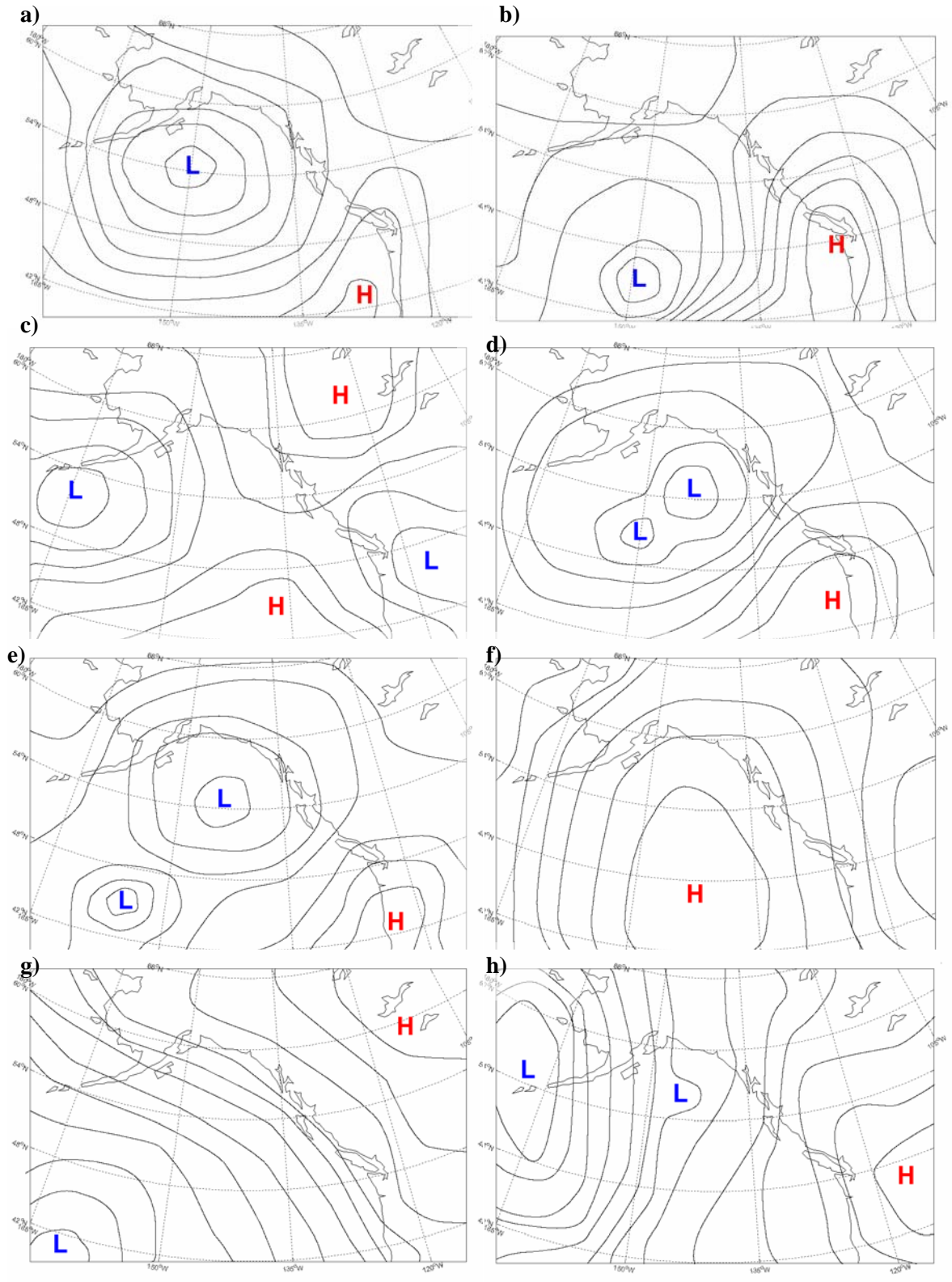


Figure 7. Schematic diagrams of synoptic map-type classes. (a) through (h) represents Class A through H, respectively. L is low pressure and H is high pressure. Black lines are representative isobars. Uses MATLAB code by R. Pawlowicz (2009).

4.3 Synoptic classification and characteristics of CLOSs

In total, 75 cases were classified out of the initial 90 selected. Of the 15 voided cases, ten were deemed to have a weak or problematic backscattering signal, and four were “unclassifiable” as determined by the map classification scheme. The remaining 75 cases were placed into the eight main synoptic classes. Most CLOSs were associated with Class A, and the fewest in G and H. The distribution of classes is shown below in Table 2.

Table 2. Summary of map class distribution.

Class	# of cases	% of analysed dataset
A	24	32.0
B	16	21.3
C	8	10.7
D	7	9.3
E	4	5.3
F	12	16.0
G	2	2.7
H	2	2.7

Most CLOSs were associated with low pressure fields (classes A – E), accounting for nearly 79% of the analysed cases. This result is not surprising, as most CLOSs do indeed end in precipitation (Figure 8) which is primarily caused by the passage of cyclonic, low pressure system.

CLOSs associated with high pressure fields (Class F) only accounted for 16% of the analysed cases. Though high pressure indicates subsidence and clear skies, nearly 42% of Class F cases did end in precipitation (Figure 8). Further analysis of this phenomenon is presented in section 6.1.

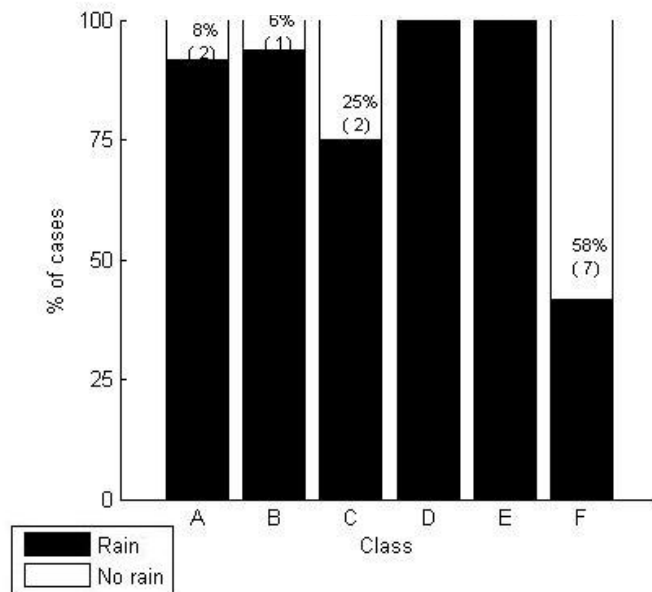


Figure 8. Distribution of CLOS cases that ended in precipitation for each synoptic map-type class. The percentage of cases per class that did not end in precipitation is given above each bar, with the number of cases in brackets.

Classes G and H were assumed to be underrepresented due to the short time series analysed and were not initially removed from the dataset because of their distinctiveness from other synoptic map classes. Given a longer time period of data, there may be more CLOSs associated with the G and H synoptic features. Nevertheless, for the purpose of this study, Classes G and H will be ignored in any subsequent analyses.

Furthermore, the unclassifiable and weak signal cases should not be neglected entirely, as significant weather events (precipitation) may occur during these CLOSs. Though some SLP maps were not necessarily classifiable, given a longer study period another synoptic map class may be developed. Weak lidar signals resulting in ambiguous signatures may have been a result of system malfunctioning (e.g. sporadic measurements resulting in a sparse signature) or significant vertical attenuation by low-level cloud cover. Though not readily interpreted in the context of this study, weak signals may still be discernable in quantitative/automated detection methods in the future.

Shape-types associated with CLOSs from all main classes showed few significant trends (Figure 9). All classes included L and R shape-types. Linear (L) types were most dominant for Classes A, B, C and F. Notably, Class F showed a distinct distribution for only linearly-associated shape-types (L, M, or R).

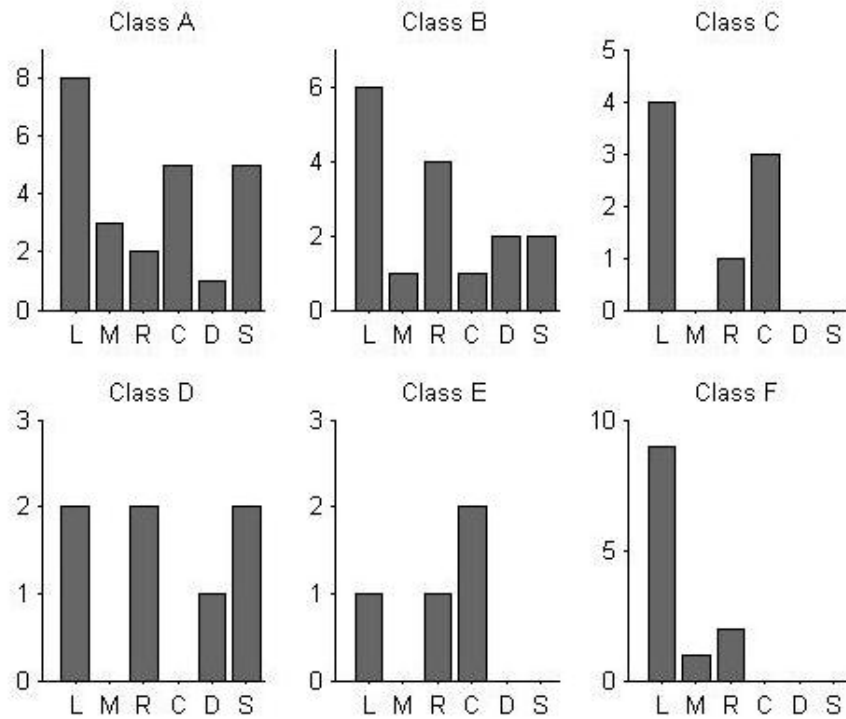


Figure 9. Distribution of shape-types by class. L (linear), M (more than one linear feature), R (re-lowering), C (concave upwards), D (concave downwards), and S (S-shaped).

There is a noticeable seasonal distribution amongst the synoptic map classes (Figure 10). Class F is dominant in the spring and summer seasons, which is most likely explained by: (1) the dominating North Pacific High in summer months, and/or (2) the Gulf of Alaska exhibiting a “blocking high” pattern (e.g. Rex block). Though maximum precipitation in Vancouver, and thus associated low pressure systems, are typical for the fall and winter months, Classes A – E did not distinctly display this trend (Figure 10). Class B and E did exhibit a fall peak, but the results may be caused by the time series chosen for analysis (more spring and summer months are represented in the catalogue of CLOSs).

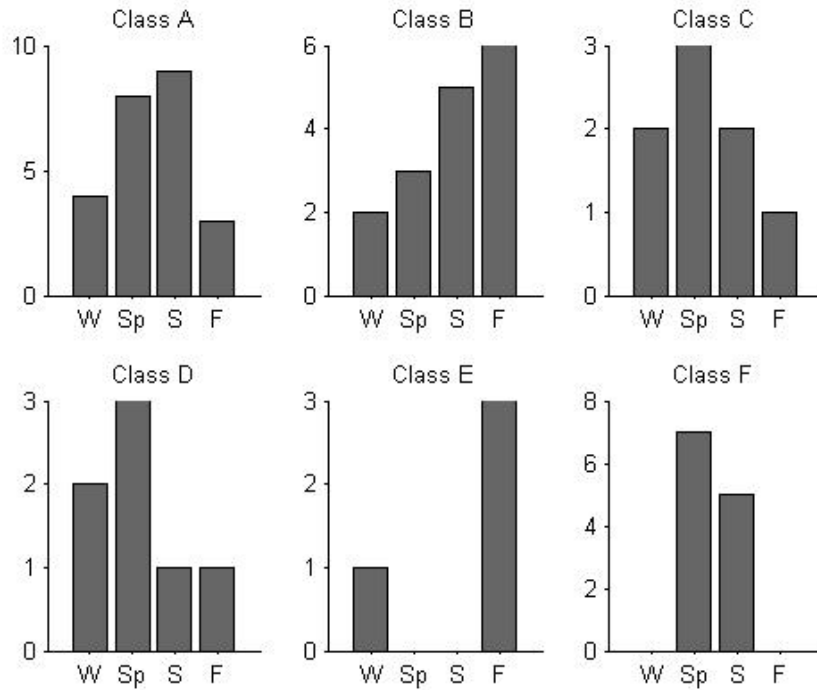


Figure 10. Seasonal distribution of cases for each class. W = Winter, Sp = Spring, S = summer, F = fall.

5.0 CLOS LIDAR PARAMETERS

5.1 Methods and analysis

Between-group variability was effectively established by the synoptic map typing scheme generated in section 4.2. Thusly, all other variables were analysed *within* the classes.

From the catalogue of CLOSs, the total lowering of cloud-base for each CLOS was calculated, by subtracting the assessed cloud-base height at the end of the CLOS from that at the beginning. Total lowering was defined as a positive value, by convention. The total

CLOS duration, or ‘lead time’ to precipitation onset, was also calculated from the subjectively extracted data (end time of lowering minus start time of lowering; as in Figure 5). From this, only a *linear* rate of lowering (RL, m/h) was calculated, thereby ignoring any effects of shape-type.

A good first-approximation of the linear RL and the starting cloud-base height is evidently available at the start of a CLOS. Thus, both of these variables were chosen as the main “predictors” for precipitation onset. The following relationships were investigated: (1) RL versus lead time, and (2) starting cloud-base versus total lowering. These two relationships were analysed in nonlinear and linear regression models, respectively.

(1) For the RL versus lead time, a nonlinear regression model was implemented independently for each class, using a least-squares estimate (where SSE, the Sum of Squares Error, is minimized, and $\alpha = 0.05$ for parameter estimates). The RL was chosen as the predictor, whereas lead time was selected as the response. Regression models failed to be visually and statistically valid for Class C. This may be due in part to the within-group variability; visually, Class C exhibited the most variability in its map classification results compared to all other groups. Additionally, Class E was not analysed because of the small number of data points generated from this group ($n = 4$). The remaining classes (A, B, D, F) all exhibited a distinct asymptotic-like decrease of lead time with respect to RL, as seen in Figure 11. In each subplot, the original data extracted from the CLOSs and the nonlinear regression models are plotted. A summary of the model equations and parameters for each class is shown in Table 3.

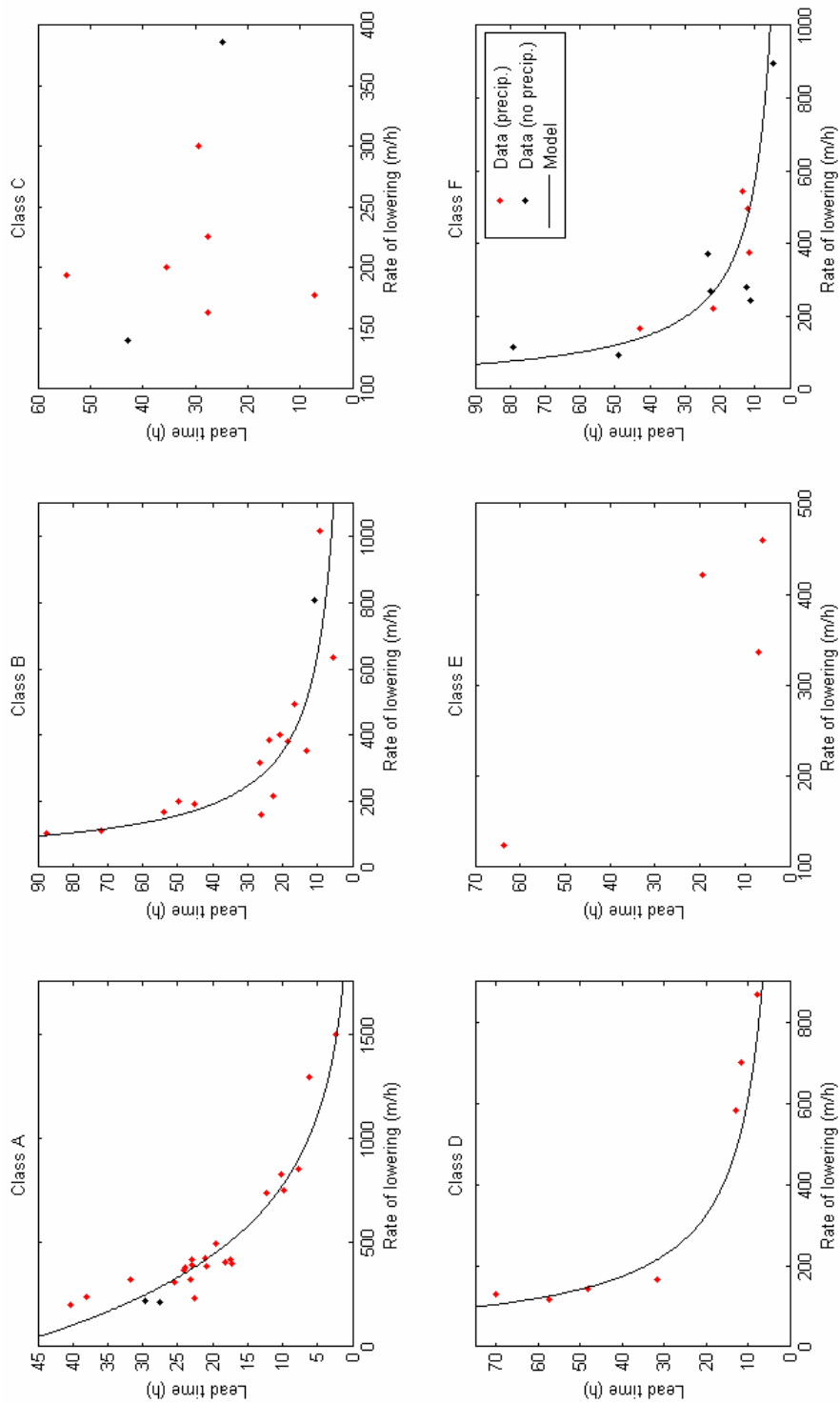


Figure 11. Plots for rate of lowering (RL) and lead time of CLOSs by class. The modelled fits are plotted in black for classes with statistically valid results.

Table 3. Nonlinear regression results for lead time response to rate of lowering (RL). All values and standard errors reported for parameter A are expressed to 10^{-3} . RMSE is the root mean squared error. Parameter values were generated based on the data for each class, where $n = 24, 16, 7, 12$ for class A, B, D and F, respectively, at $\alpha = 0.05$.

Class	Regression Equation	RMSE	Model		
			Parameter	Value	Standard error
A	$A \times e^{(RL \times b)}$	3.805	A	0.049	0.00483
			b	-0.002062	0.000277
B	$A \times RL^b$	8.867	A	16.033	11.300
			b	-1.140	0.140
D	$A \times RL^b$	8.506	A	11.827	17.962
			b	-1.103	0.308
F	$A \times RL^b$	11.88	A	7.137	8.128
			b	-1.035	0.229

RMSE (Root Mean Squared Error) values were relatively low for all models, providing satisfactory statistical significance for the model's predictability. Note that the prediction model for Class A is an exponential equation, and those for classes B, D and F are power equations; however, exponential and power equations may be equivalent if parameters (constants) are manipulated.

(2) For the prediction of total lowering from starting cloud-base altitude, a linear regression model was derived using the least-squares method (Figure 12). The linear model was constrained to the zero x - and y -intercept (0,0). Logically, if the starting cloud-base altitude of a CLOS is at ground level ($x = 0$), there cannot be any lowering to follow ($y = 0$). Models for classes A, B, C and E showed high R^2 (coefficient of determination) values (Table 4). The model for Class D only produced an R^2 value of 0.55, and Class F failed to show any significant model predictability. Also provided are the F calculated and critical values produced using an ANOVA on the overall modelled fits. All models showed statistically significant predictability.

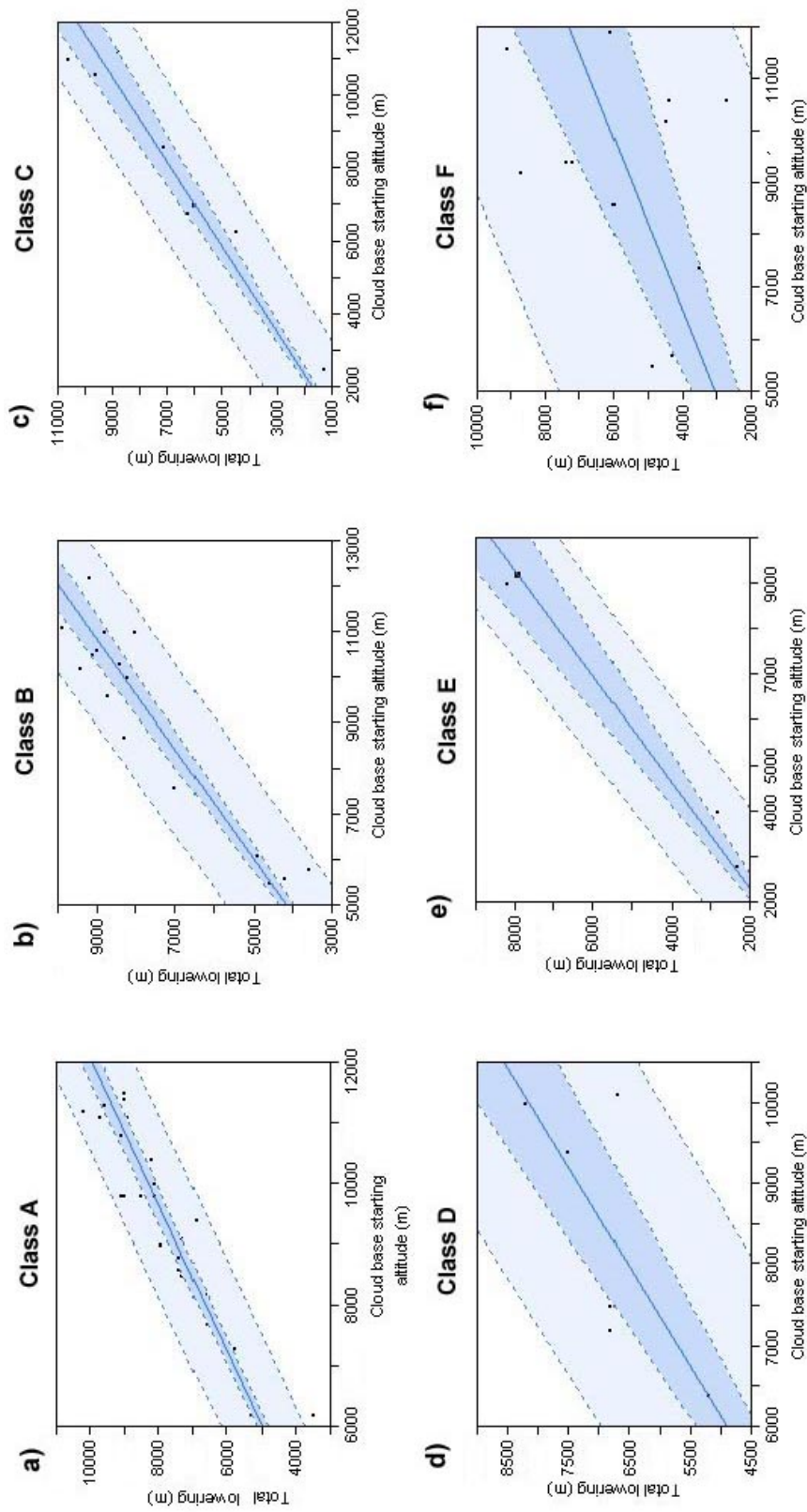


Figure 12. Plots for cloud-base starting altitude versus total lowering for each CLOS, by synoptic map class. Collected data are represented by black points. The modelled line of fit is in dark blue. The areas shaded in darker blue represent the 95% confidence of fit of each model, whereas the areas shaded in lighter blue represent the 95% confidence of fit of predictable data. Generated using JMP.

Table 4. Linear regression results for total lowering response to initial cloud-base height. All models are in the form $y = 0 + cx$, where y is the predicted total lowering of the CLOS, and x is the initial cloud-base height. All models and statistics were generated using a standard confidence level of $\alpha = 0.05$, and $n = 24, 16, 8, 7, 4,$ and 12 for Class A through F, respectively.

Class	Model				
	R ²	Coefficient (c)	Standard Error	F statistic	F critical value
A	0.86	0.8330413	0.012475	4458.865	<0.0001
B	0.88	0.8333927	0.019083	1907.253	<0.0001
C	0.94	0.8602641	0.031566	742.7157	<0.0001
D	0.55	0.8163373	0.034845	548.8695	<0.0001
E	0.98	0.86616	0.03318	681.4482	0.0001
F	–	0.6103049	0.062862	–	–

5.2 Synthesis

(1) The nonlinear regression models for predicting the lead time of precipitation onset from the RL did indeed produce statistically significant results. As well, the asymptotic-like decreases of lead time with respect to rate of lowering are logically sound; it is assumed that an RL of 0 m/h would not result in any CLOS and thus a seemingly infinite lead time. The models produce varied predictions of lead time based on an initial input RL. For example, if an initial linear RL of 400 m/h were deduced from a CLOS, a Class A synoptic-type would result in the longest lead time prediction, whereas a Class F synoptic-type would result in the shortest (Table 5).

Table 5. Hypothetical model predictions for CLOS lead time based on an initial input RL of 400 m/h. The synoptic map classification determines the model to be used for the calculation.

Class	Predicted lead time (h)
A	21.78
B	17.27
D	15.94
F	14.49

(2) The linear models fit to predict the total lowering of a CLOS in each class also gave a good indication of what the end-time cloud-base height may be before the onset of

precipitation. Overall, >85% of the data for classes A, B, C and E can be explained by the linear regression models, with statistically significant positive relationships between starting cloud-base height and total cloud-base lowering. In combination with the lead time predictions from the nonlinear regression models, a better estimate of precipitation onset should be deducible (see Chapters 7 and 8)

5.3 Relations between CLOS lidar parameters and other meteorological data

The CLOS predictors derived from lidar imagery (RL and starting cloud-base height) were plotted against other acquired meteorological data, including: SLP, 500 mb wind speed, and 3-hour pressure change and the categorical pressure tendency. There was no evidence of any statistically significant relationships between any of the variables. However, Figure 13 shows a windrose of 500 mb level winds for all low pressure fields (classes A – E), indicating a predominant westerly component. This is consistent with the general nature of low pressure systems across the Pacific Ocean, with a west-to-east development and storm track. Thus, it is expected that precipitating systems associated with synoptic map classes A – E are “steered” to the east, towards Vancouver.

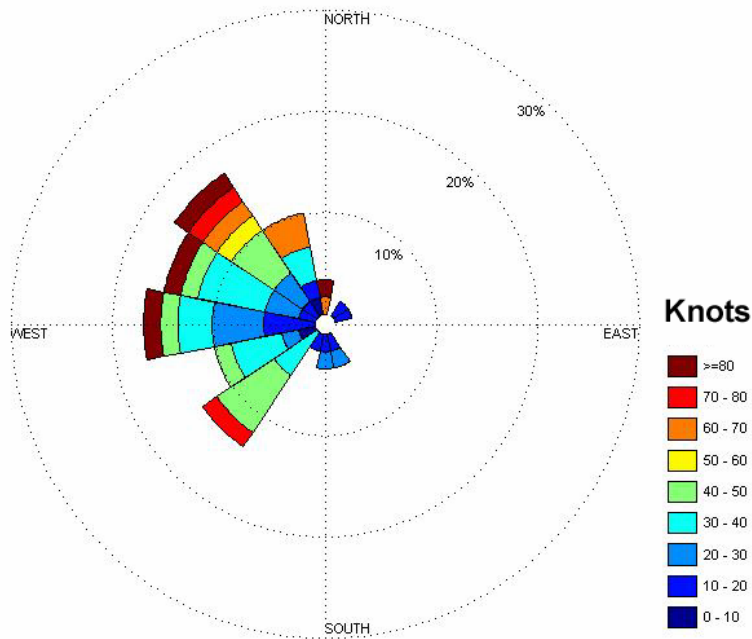


Figure 13. Windrose for all low pressure map classes (Class A – E). Using a polar coordinate system, the frequency of wind directions are plotted, where the circular grid represents the percentage of the dataset of a particular direction. Colour bands represent the wind speed (in knots). The longest spoke(s) shows the dominant wind direction(s). Generated using MATLAB code by *Anonymous* (2009).

6.0 SUBJECTIVE PREDICTORS

Evidently, there are some limitations to the regression models in handling particular synoptic map-types and potentially problematic (non-linear) shape-type features. Specifically, (1) Class C failed to result in a statistically significant regression model for the crucial prediction of lead time, (2) Class F not only resulted in the most cases of CLOSs ending without precipitation, but also failed to provide a prediction model for total CLOS lowering, and (3) in a real-time nowcasting situation, shape-types of the cloud-base lowering appearing over time are difficult to handle effectively in the linear fashion required by the models (particularly M and R signatures). Following the analysis of the initial map-typing results and CLOS lidar parameters, these problems were subjectively (visually) investigated.

6.1 Class C

When all SLP maps for Class C were manually re-examined, there was evidence of larger within-group variability than previously considered by the synoptic map classification scheme. Though the relationship between RL and lead time data did not generate a model for this class, it is worthwhile noting that the data does fit well within the asymptotic-like bounds and total scatter data when all classes are considered (Figure 14).

To determine the probable causes of Class C's relatively high proportion of CLOSs that did *not* result in precipitation, the SLP maps were re-examined. It was found that cases that did not have a distinctive col of pressure ("blended" highs), or whose central col axis was located onshore resulted in precipitation (Table 6). The "blended" high pressure ridges tend to move northward, allowing smaller low pressure systems to trail behind, or for low pressure systems to develop over northern WA and impact Vancouver. Conversely, when the central axis of the col was located west of the coastline, the CLOS did not result in precipitation. The initial CLOS signature was most likely marked by the low pressure system

over northern WA, whilst precipitation was suppressed by the southerly region of high pressure moving northwards and expanding over the west coast, causing subsidence.

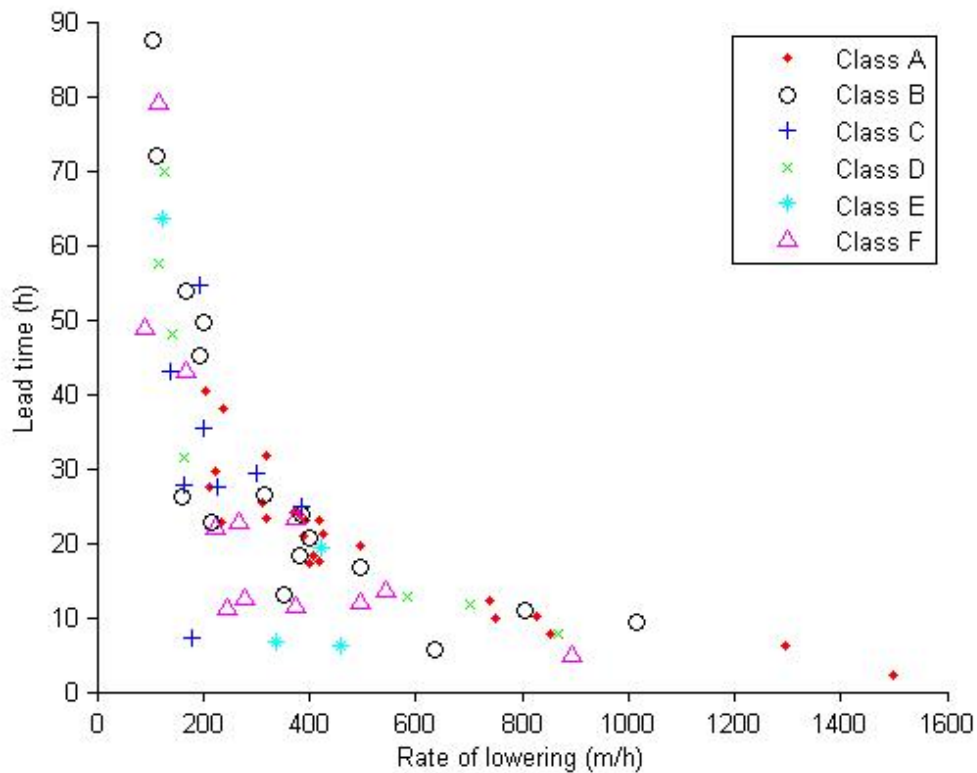
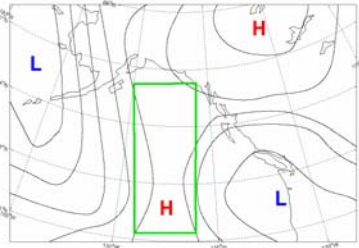
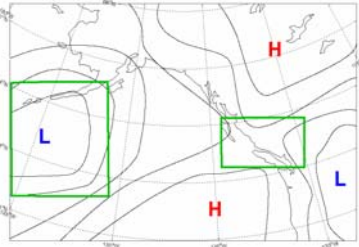
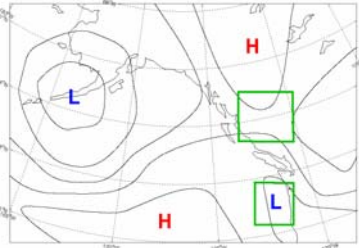
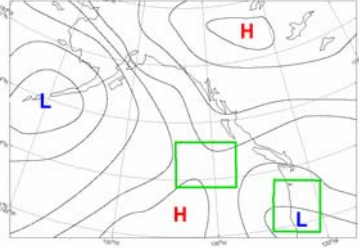
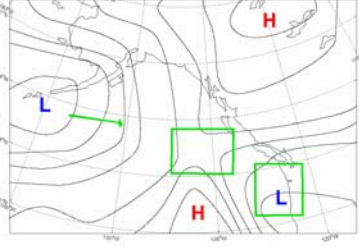


Figure 14. Plot of rate of lowering (RL) (m/h) versus lead time (h) for all synoptic map-type classes. Note that data for Class C falls within the total scatter of all data.

Whether or not these results are conclusive enough to lead to another synoptic map class would need to be investigated given a longer data set. However, the explanations provided here should be substantial given that several cases exhibited the same features leading to the onset or lack of precipitation at the end of a CLOS.

Table 6. Subjectively determined features of all Class C cases which may or may not lead to precipitation onset. The CLOS number in the left-hand column corresponds to the catalogue number (Plate A). Characteristic features of influence for onset of precipitation are denoted in green on the schematic SLP diagrams. Illustrations uses MATLAB code by R. Pawlowicz (2009)

CLOS case #	Date	Characteristic	Example illustration
RESULTING PRECIPITATION			
1 82	April 20 – 21, 2008 July 3 – 6, 2009	‘Blended’ highs (no distinct col) Low pressure systems may develop over northern WA	
13 56 60	July 25 – 26, 2008 March 8 – 9, 2009 March 25 – 26, 2009	Col onshore Primarily influenced by low pressure system to the west	
31	November 3, 2008	Col onshore Primarily influenced by low pressure system over northern WA	
NO PRECIPITATION			
46	January 24 – 25, 2009	Col offshore Clouds associated with low pressure system over northern WA	
53	February 9 – 10, 2009	Col offshore Cloud cover initially influenced by low pressure system over northern WA, then by passage of initially westerly located system	

6.2 Class F

Figure 8 demonstrated that Class F had the largest proportion of CLOSs that did not result in precipitation. Though the data from this class was well handled by the nonlinear regression model for lead time prediction, ancillary data would be useful in nowcasting the likelihood of precipitation from a Class F map-type. Investigation provided evidence that the starting cloud-base height could be a good predictor for the likelihood of precipitation. An ANOVA revealed that CLOSs that did not result in precipitation started at statistically significant higher altitudes. Details of the analysis are provided in Table 7 below.

Table 7. Results of the ANOVA for starting cloud-base heights partitioned by onset of precipitation or lack thereof. Y = yes, N = no precipitation, where $n = 5$ and 7 , respectively. A standard significance level of $\alpha = 0.05$ was used.

Precip.?	Mean cloud base starting altitude (m)	Standard deviation	95% confidence interval		F statistic	F critical value
N	10214	1528	8801	11627	6.1644	0.0324
Y	7720	1964	5281	10159		

CLOSs that started at higher altitudes indicated initial high cloud structure (e.g. cirrus, cirrostratus). A subsequent examination of the SLP maps was consistent with this finding. In fact, most Class F CLOSs that did not result in precipitation exhibited the passage of weakening frontal structures or weakly developed low pressure systems. Thus, the cloud decks associated with these structures and systems manifested as a CLOS, but failed to precipitate due to cyclolysis onshore, upper cold front passages, or weakly developed cloud structure. A detailed analysis of these cases is provided in Table 8

Furthermore, Table 8 details those CLOSs that began at lower altitudes and ultimately resulted in precipitation despite dominating high pressure conditions. Lower cloud structures are indeed present and increase the likelihood of conditions leading to precipitation. The main features from the high pressure fields of Class F that ultimately resulted in precipitation were both systematic errors of the map-typing procedure, and atmospheric development. Due

Table 8. Detailed features of all Class F cases which may or may not lead to precipitation onset. The CLOS number in the left-hand column corresponds to the catalogue number (Plate A). The primary characteristics of the pressure fields on associated SLP maps are categorized as follows: NIF (“not in frame”, a system is present beyond the map frame of the originally classified SLP map), OSD (onshore development), WS/WF (weak system/weakening front), NI (cloud structure not intercepted by Vancouver).

Primary Characteristic	CLOS case #	Date	Details
RESULTING PRECIPITATION			
NIF	6	May 18 – 19, 2008	Low pressure located south of map frame limits and moves northward
	9	June 18 – 19, 2008	Low pressure trough moves from south of map frame limits; a low pressure system is also undergoing cyclolysis in the Gulf of Alaska which was not dominant on the initial SLP map
	79	June 20 – 21, 2009	Low pressure system located west of map frame limits move eastward
OSD	7	May 25 – 26, 2008	An initial shortwave low pressure trough creates extended cloud cover, with low-level cloud cover moving over Vancouver from the east. Possible topographic forcing.
	57	March 8 – 9, 2009	Onshore development and movement of a low pressure system, most likely associated with the polar front. Possible topographic forcing.
NO PRECIPITATION			
WF/WS	67	April 24 – 25, 2009	Weakly developed front incoming from very high northern latitudes
	73	May 20 – 21, 2009	Development of very weak low pressure system by a cut-off low in the Gulf of Alaska
	83	July 20, 2009	Occluded front with weakening cirrus clouds followed by the passage of a high pressure system
OSD	68	April 26 – 29, 2009	Passages of upper cold fronts from northern latitudes initial the CLOS. Onshore development of a low pressure system via shortwaves and subsequent stagnation over the southern portion of BC.
	75	May 31 – June 2, 2009	Development of low pressure trough onshore over southern BC and associated dissipation of cloud deck
	77	June 11, 2009	Onshore stagnating local low pressure systems and associated stationary front
NI	88	August 16 – 17, 2009	Passage of a broad warm front cirrus deck but no precipitation bands intercept Vancouver

to constraints imposed by the literal frame of the SLP map (extent of the longitudes and latitudes represented), some low pressure systems located around the extremities of the dominating high pressure regions may have been missed. One suggestion to remedy this in a real-time nowcasting situation would be to more carefully examine the complimentary IR satellite imagery, or perhaps use larger map coverage to better encapsulate all synoptic scale features. Otherwise, onshore development of localized low pressure systems, in possible combination with topographic forcing, may result in precipitation. Since onshore development of low pressure systems and troughs was present for both precipitating and non-precipitating Class F map-types, a careful analysis of the probability of associated precipitating clouds is necessary.

6.3 Problematic shape-types

The data extracted from the lidar imagery and resulting models were based only on the resultant linear RL of all CLOSs. Thus, non-linear shape-types may prove problematic when the models are implemented in real-time. Of most concern are the M (more than one linear feature) and R (re-lowering) shape-types, due to their initial apparent linear structure. Effectively, this may cause the nowcaster to produce a lead time much under the actual lead time.

As guidance, M shape-types distinctly exhibit a cirrus cloud deck as the secondary lowering feature aloft. This may be readily inferred from hourly METAR data. The resulting nowcast should be extended to encapsulate the end of the secondary lowering feature.

Even more challenging is the handling of R shape-types. As opposed to an M shape-type, R signatures exhibit a distinct time delay between the first and second lowering features. This may lead a nowcaster to believe that no precipitation will ensue at the end of the first signature, when in reality the associated precipitating system has not yet passed and a secondary lowering will follow. As the first signature does not result in precipitation, lower-level precipitating clouds should be not present at this time. Inferred from hourly

METARs, lower-level cloud structures end the first lowering signature, but have low opacity (e.g. AC3, altocumulus with 3/8 opacity).

7.0 DECISION TREE IMPLEMENTATION: “A USER’S GUIDE”

Based on the methods undertaken in this study, the real-time use of lidar imagery to nowcast the timing of precipitation relies on two main steps once the nowcaster has recognized a CLOS: (1) manually classify the current SLP map, and *then* (2) use climatological CLOS regression relations to forecast timing of precipitation onset.

The regression models should effectively provide a best “first guess” of the lead time to precipitation onset. Many manual adjustments can be made by visually assessing the progression of the CLOS and examining any of the subjective predictors from Chapter 6, if applicable. The primary requirement in any lead time prediction is intercepting a *linear* RL. Furthermore, any adjustments to the lead time estimate should be done using the same model that corresponds to with the *initial* map-type, as determined by the classification scheme. In summary, a few general steps should be followed:

- 1. Identify a CLOS on lidar imagery.** Cloud-base lowering must be apparent. Some discretion may be needed for weak or sporadic backscattering signals. Assessing the lidar’s functional state may be done to evaluate the quality of the output image used for interpretation.
- 2. Obtain the SLP map** that best matches the start time of the CLOS and **classify** the map based on the derived map classification scheme (Decision Tree (DT) Page 1, Figure 15a)
- 3. Make a best-guess of the linear RL** of the CLOS. Using an initial 3-hr lead time for estimation should be used as a “first guess”
- 4. Use the RL assessed in Step 3** as input for the nonlinear “**Lead time Prediction**” model for the appropriate map class (DT Page 2 – 3, Figures 15b and c)
 - a.** As the CLOS progresses, recalculate the linear RL by subtracting the **current** cloud-base height and time from the **initial** cloud-base height and time, respectively, and reemploy the lead time model

- b.** If applicable, use the additional **subjective predictors** to adjust the lead time estimate as necessary (DT Page 4, Figure 15d)
- 5.** If the model fails to give any reasonable results, **visually assess the CLOS** and assume that precipitation will occur when the CLOS reaches the altitude determined by the “Total Lowering” model (DT Page 2 – 3, Figures 15b and c)

The initial first-guess of the linear RL requires some time to elapse before the nowcaster can efficiently perceive the CLOS. However, the synoptic SLP map should always correspond as close as possible to the initial onset of the CLOS, *not* to the time that the nowcaster “sees” that there is cloud-base lowering. Monitoring the CLOS over time is a necessary component of nowcasting the onset of precipitation, as shape-types are not often evident at the onset of a CLOS.

Figure 15 is the resultant DT based on the manual map classification scheme, regression models, and subjective predictors as discussed in Chapters 4 through 6.

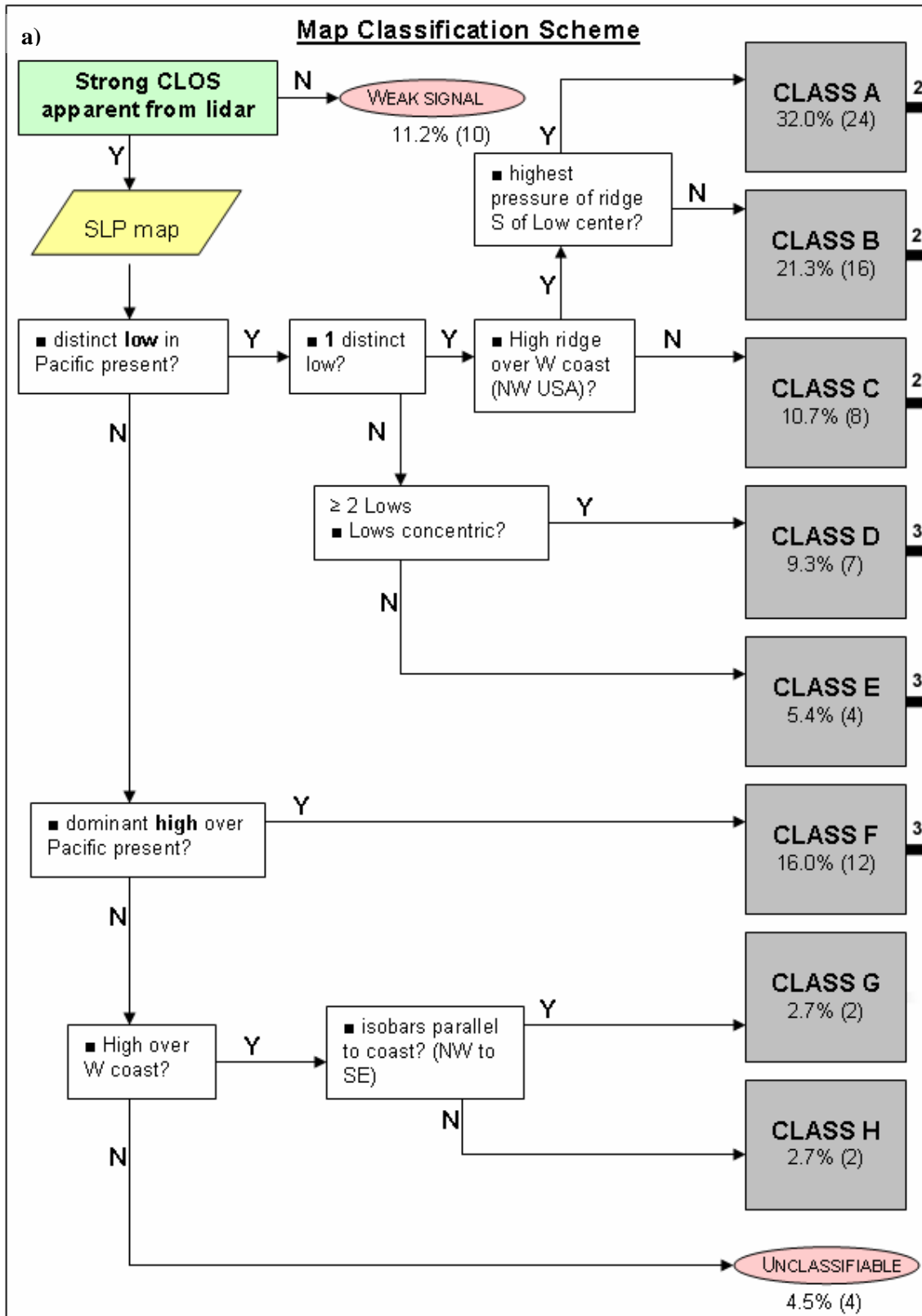


Figure 15 a). Decision tree for nowcasting precipitation onset. **Page 1:** Map Classification Scheme. Percentages in the grey boxes indicate the likelihood of classifying a CLOS to that map-type. The numbers in brackets refer to the actual number of cases used to derive the model. Solid lines are decisions that must be taken. The number above the arrow heads indicates the next page to follow.

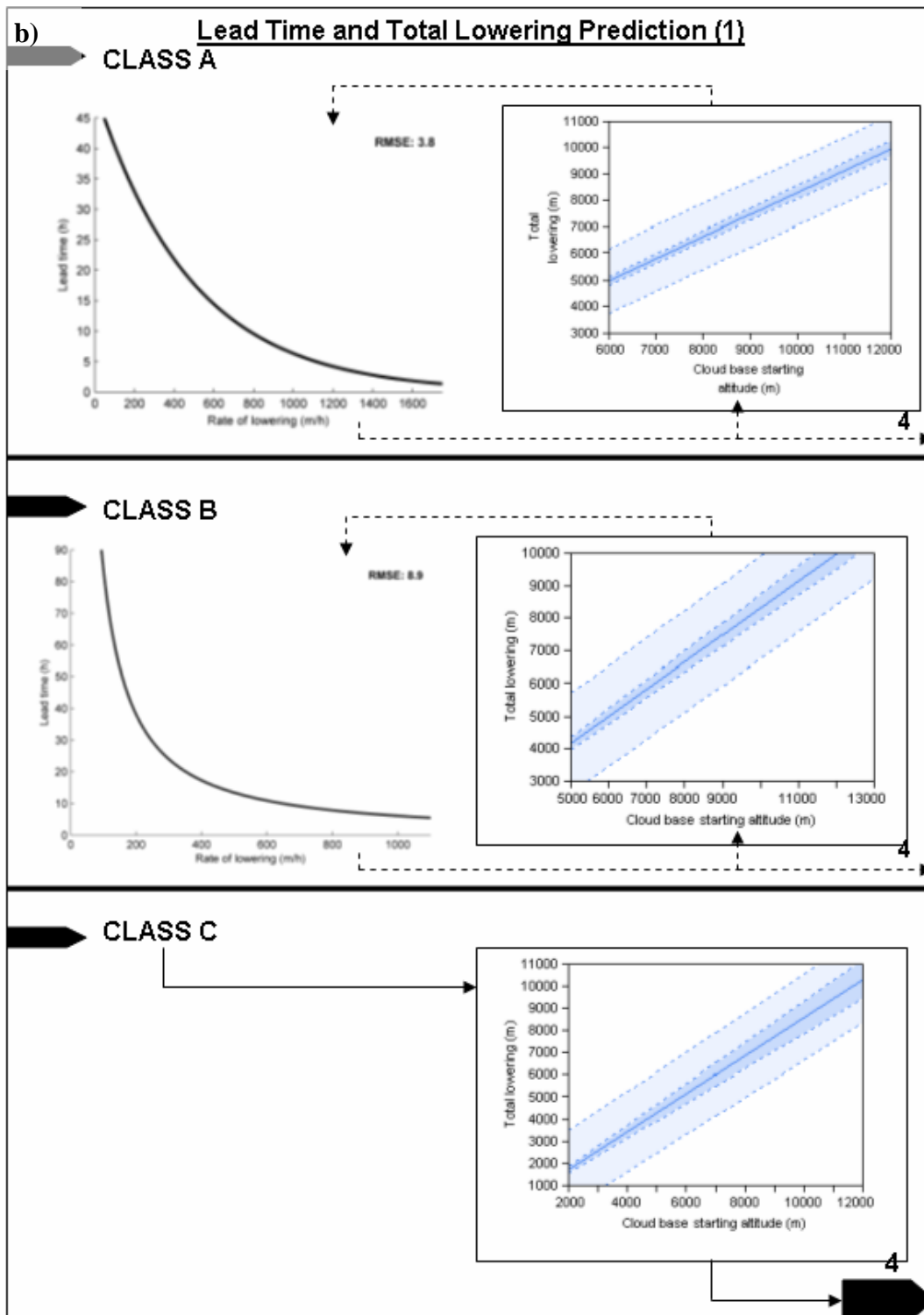


Figure 15 b). Decision tree for nowcasting precipitation onset. **Page 2:** Lead time and total lowering prediction (1), for classes A – C. Large black arrows are connectors to other pages of the DT. Solid line arrows indicate decision paths that must be taken. Dotted line arrows indicate paths that may be taken if needed. The number above the arrow heads indicates the next page to follow.

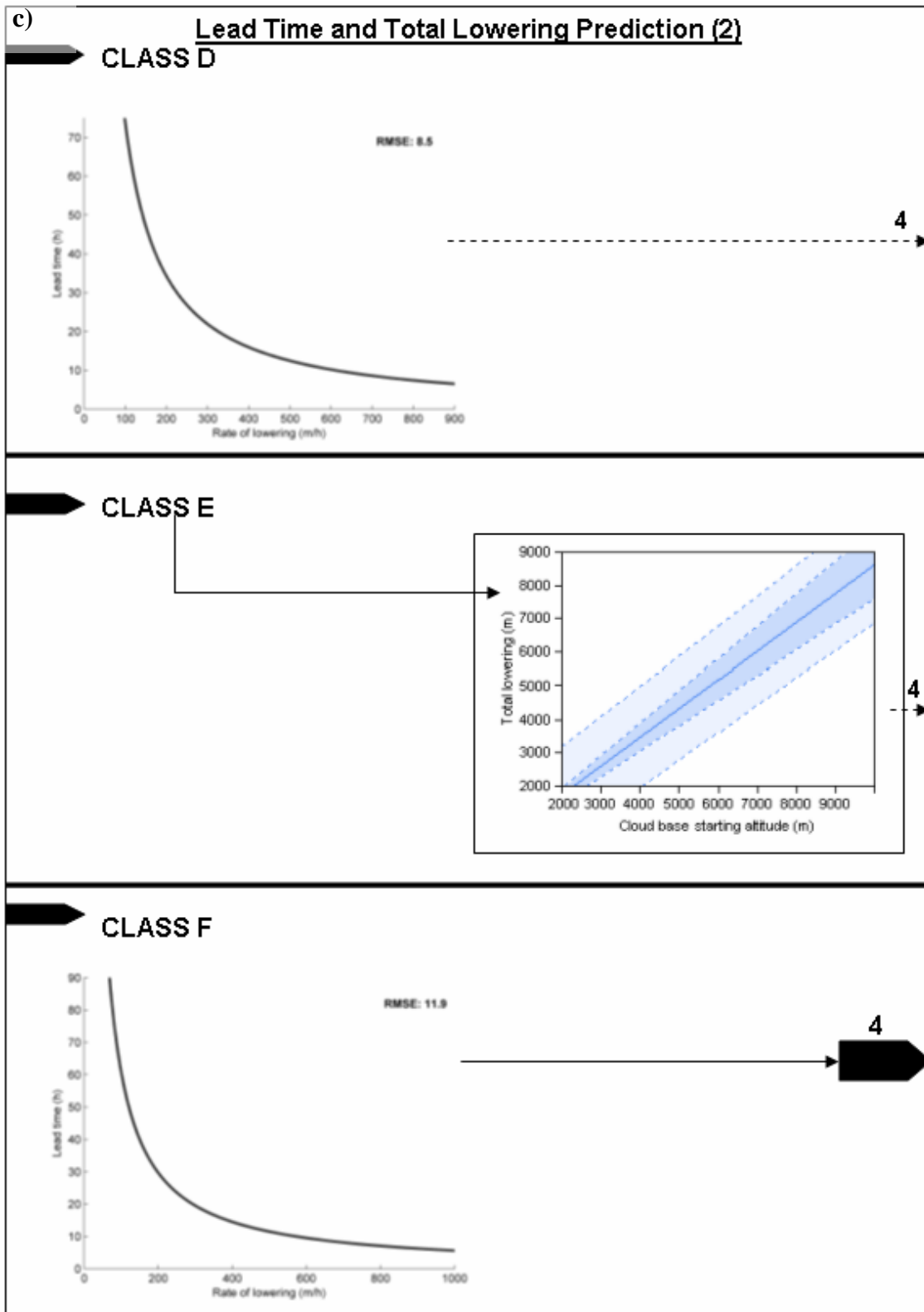


Figure 15 c). Decision tree for nowcasting precipitation onset. **Page 3:** Lead time and total lowering prediction (2), for classes D – F. Notation is consistent with Figure 15 (b)

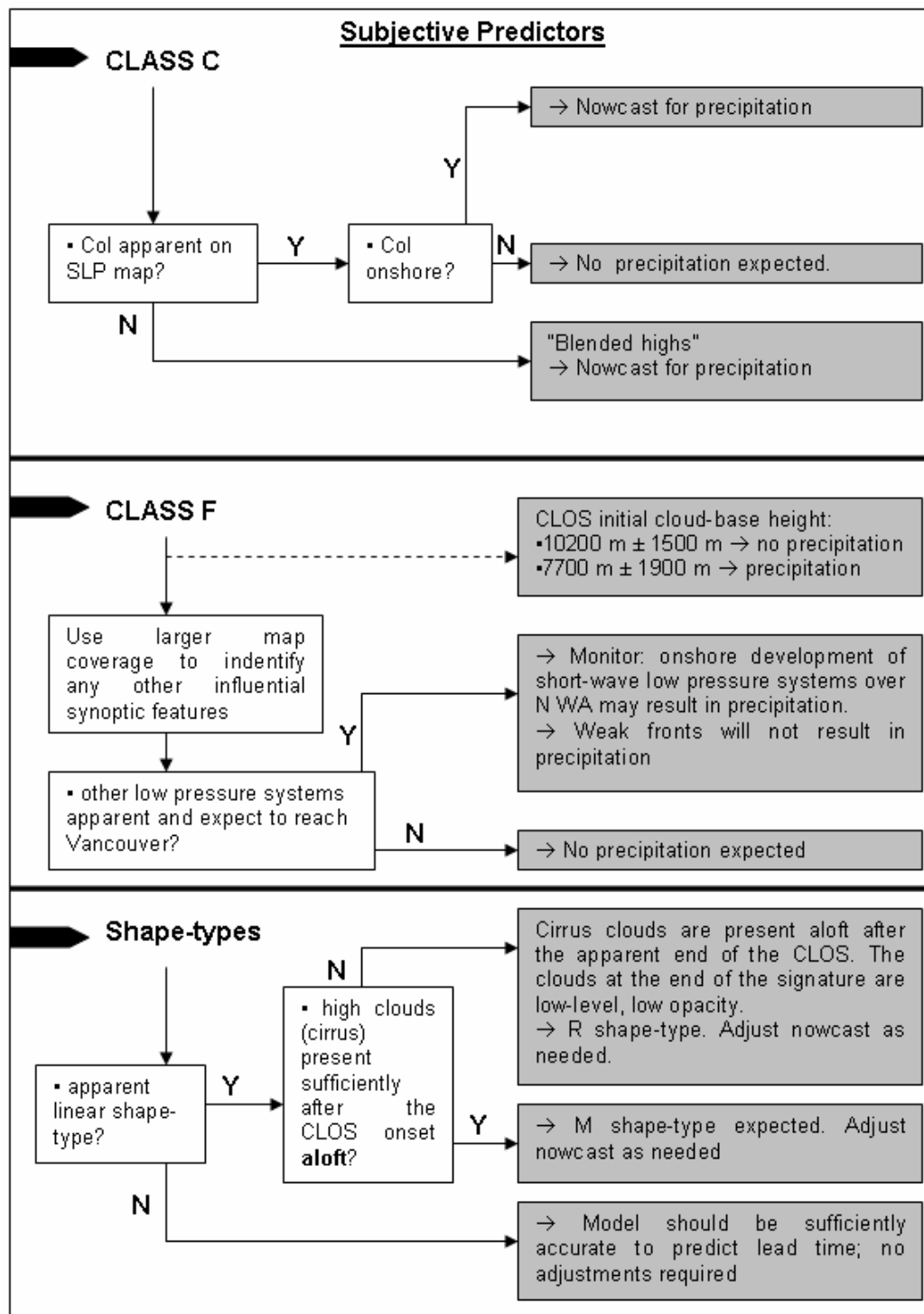


Figure 15 d). Decision tree for nowcasting precipitation onset. **Page 4:** Subjective predictors. Notation is consistent with Figure 15 (b)

8.0 NOWCASTING PRECIPITATION ONSET: MODEL VALIDATION

8.1 Introduction

In this chapter, the forecasting approach and DT described in the previous section is applied to a small set of independent, randomly selected CLOS cases in order to evaluate the utility and overall accuracy of the model. The following constitutes a preliminary assessment, as only seven cases are examined from the time period following that of the initial CLOS catalogue. Many more cases would need to be considered in order to provide a more rigorous statistical assessment based on standard meteorological skill scores and validation statistics (e.g. Forecast Skill, SS; False Alarm Rate, FAR).

8.2 Approach to validation

Based on the approach described in the Chapter 7, a total of seven CLOS test cases were randomly chosen in the time period of January through April, 2010. These CLOSs were all clearly identifiable in real-time shortly after their onset. For each case, various lead time estimates were produced by recalculating the linear RL over three different time periods. The “first-guess” RL was calculated 3 hrs after the visible onset of the CLOS and used to initiate the lead time prediction model (Method 1) (DT page 2 – 3, Figures 15b and c). Then, the initial cloud-base height was input into the appropriate prediction model for “Total Lowering” (DT page 2 – 3, Figures 15b and c). Using the time intercept of half of the predicted total lowering, a second RL was calculated and re-input into the lead time prediction model (Method 2). This process was repeated using three-quarters of the total lowering predicted (Method 3). The RL was calculated three times in order to arguably capture and effectively handle any developing shape-type features. Methods 1 – 3 are schematically presented in Figure 16. When features determined by the “Subjective Predictors” component of the conceptual model were evident (DT Page 4, Figure 15d),

adjustments to the lead time estimate were made accordingly. Results were then compared to the actual lead time to precipitation onset.

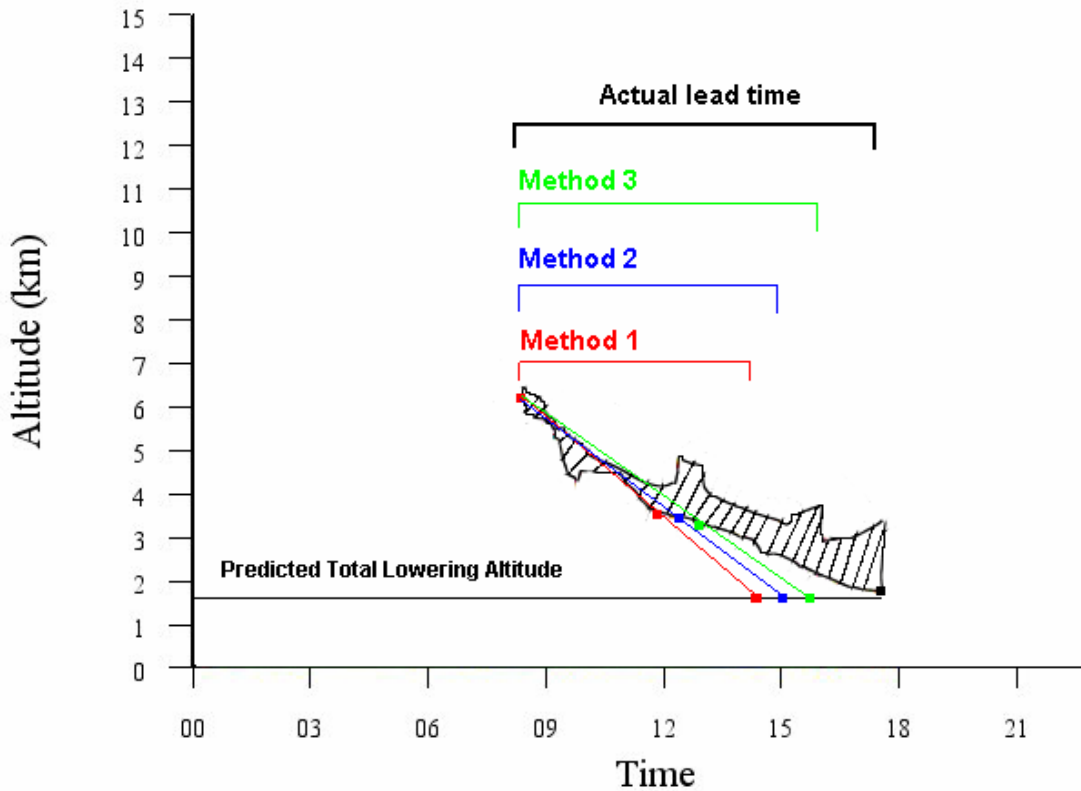


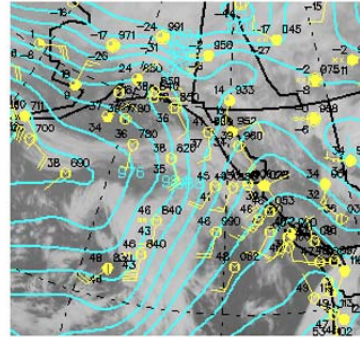
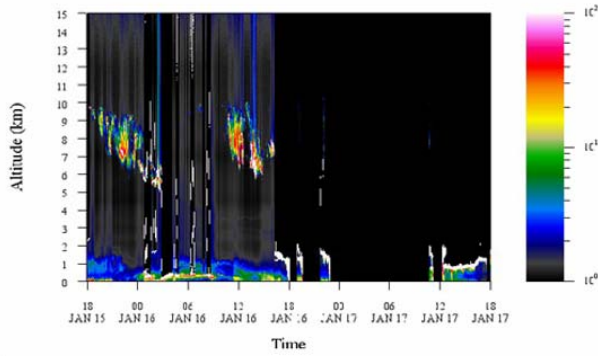
Figure 16. A hypothetical CLOS and methods used to nowcast precipitation onset. The hatched area represents cloud as measured by the lidar. Method 1 refers to the lead time produced by using a 3-hr Rate of Lowering estimate. Method 2 refers to the lead time produced using the time-intercept of half of the predicted total lowering. As in Method 2, Method 3 uses three-quarters of the predicted total lowering to nowcast lead time.

8.3 Validation results

Of the seven CLOS cases analysed, all ended in precipitation. Initial high pressure conditions (Class F) were not anticipated due to the seasonality of the test period (winter-spring). Indeed, all cases were associated with dominant low pressure conditions, and most were classified as a Class A synoptic map-type. Furthermore, no cases were considered “unclassifiable” based on the synoptic map typing scheme derived in Chapter 4. The analysed CLOSs and corresponding initial SLP maps are provided in Figure 17.

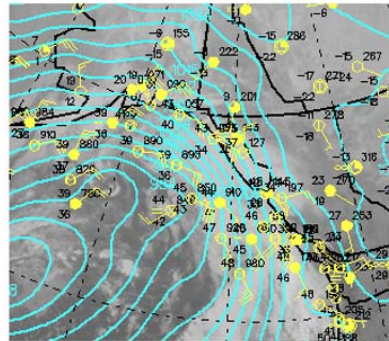
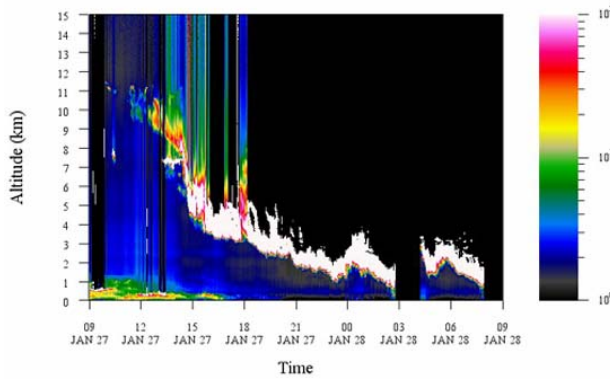
a)

Backscatter Ratio at 1064 nm from 2010/01/15 18:00:00 to 2010/01/17 18:00:00



b)

Backscatter Ratio at 1064 nm from 2010/01/27 09:00:00 to 2010/01/28 09:00:00



c)

Backscatter Ratio at 1064 nm from 2010/02/09 12:00:00 to 2010/02/10 12:00:00

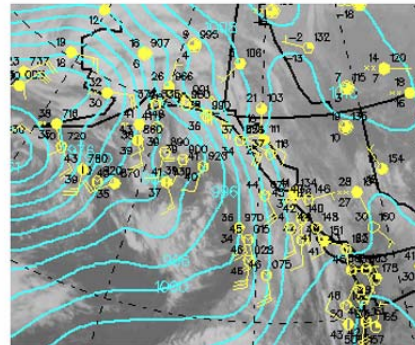
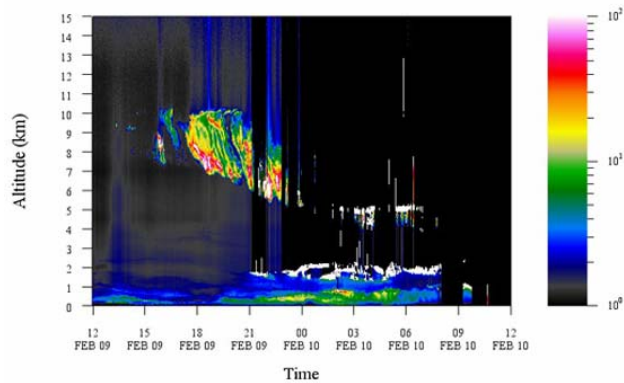
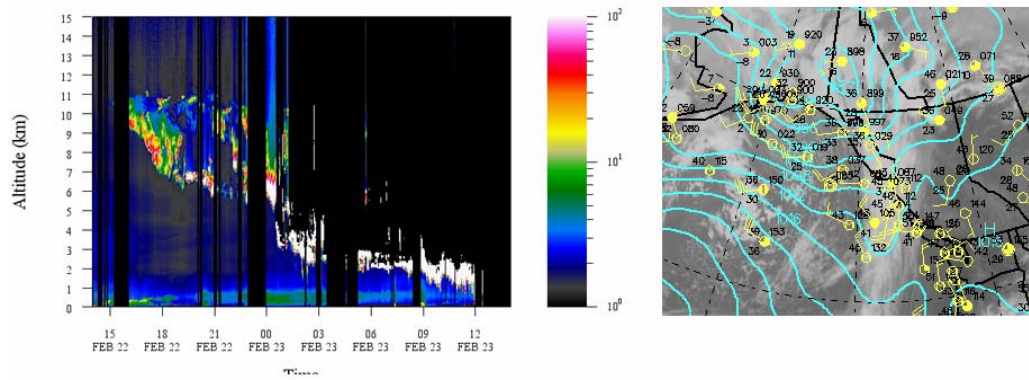
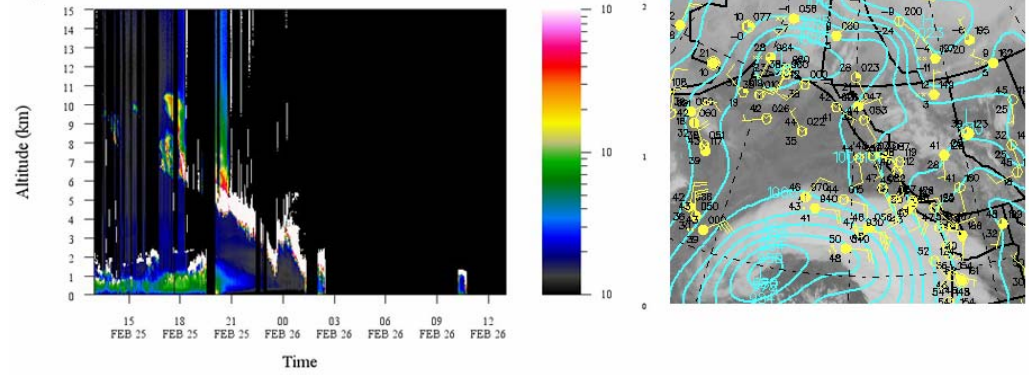


Figure 17 (a) – (c) see caption on p. 44

d) Backscatter Ratio at 1064 nm from 2010/02/22 14:00:00 to 2010/02/23 14:00:00



e) Backscatter Ratio at 1064 nm from 2010/02/25 13:00:00 to 2010/02/26 13:00:00



f) Backscatter Ratio at 1064 nm from 2010/03/06 22:00:00 to 2010/03/07 22:00:00

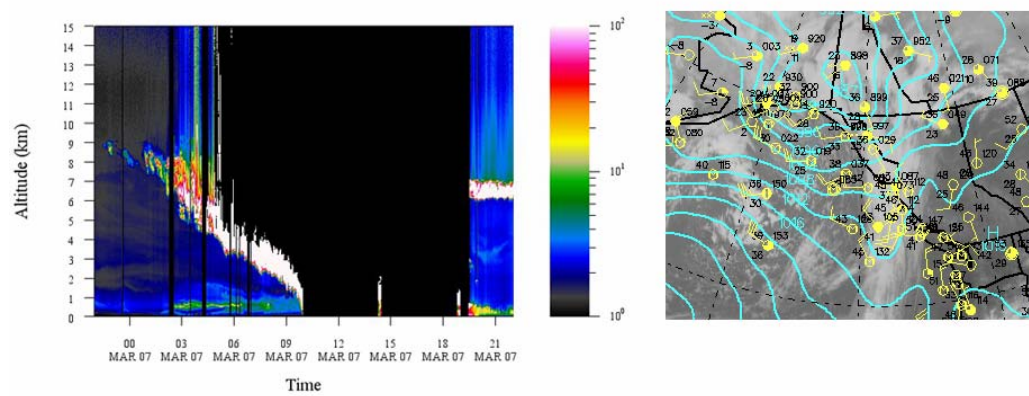


Figure 17 (d) – (f) see caption on p. 44

g) Backscatter Ratio at 1064 nm from 2010/04/04 10:00:00 to 2010/04/05 10:00:00

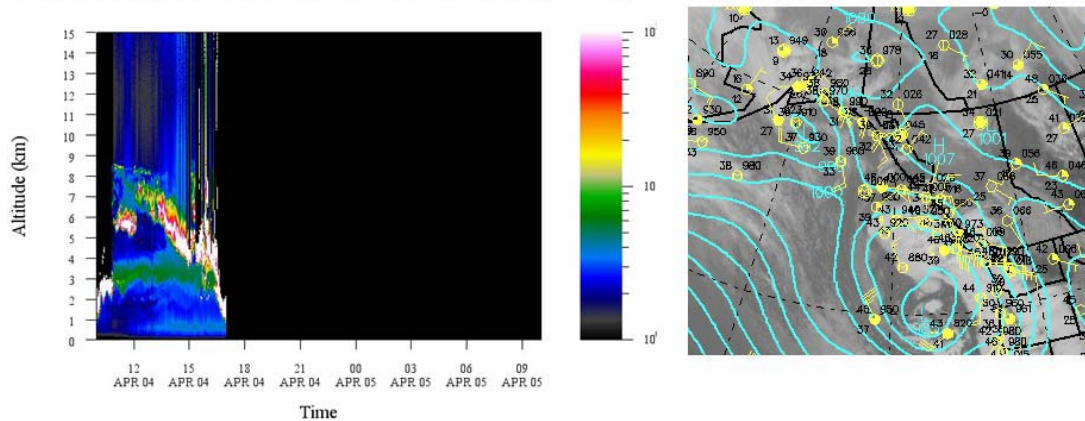


Figure 17. Resultant CLOSs from lidar imagery (left) and corresponding SLP/IR composite (right) maps used for model validation. Figures (a) through (g) represent cases *i* through *vii*, respectively. On SLP maps (right), cyan lines are isobars; yellow markers are weather stations; land is outlined in black. Lidar imagery provided by CORALNet (2010); SLP maps modified from The California Regional Weather Server (2009).

The emergence of shape-types over the course of CLOS development proved to be the most difficult feature to handle in the model. An initial shape-type was estimated three hours after the CLOS onset. The majority of initial shape-types were linear (L). Over the course of the CLOS, additional subjective features were apparent which allowed for an ‘adjustment’ of the lead time when necessary, or to discern whether or not precipitation would ensue. Nearly all of the adjustments were predictable using the “Subjective Predictors” in the Decision Tree (Table 9).

Figure 18 presents the overall lead time estimates produced with Methods 1 – 3 over the duration of the CLOS. Of the three methods used to calculate the RL, Method 3 most often provided the best lead time prediction, and on average estimated the lead time within 2.34 hr of the actual lead time. Method 2, using half the total lowering as a RL estimate, showed the most variability and least accurate prediction. CLOSs that remained linear (cases *vi* and *vii*) were predicted with greatest accuracy.

Table 9. Summary of nowcasting results using the derived model. “Nowcast error” refers to the difference between the predicted lead time and the actual lead time to precipitation of the CLOS, where positive values signify an overestimate of lead time, and negative values signify an underestimate. “Method” refers to Methods 1 – 3 for recalculating lead time. “Adjustment” refers to any prediction (“Predicted”) and usage of a subjectively derived predictor; “Needed” refers to whether or not the feature was used to adjust the prediction of lead time.

Case	Synoptic map class	Actual lead time (h)	Best predicted lead time		Shape-type		Adjustment	
			Nowcast error (h)	Method	Initial	Overall	Needed	Predicted
i	A	23.83	+ 4.57	3	L	R	×	×
ii	B	16.75	- 2.82	1	L	S	×	×
iii	A	18.75	+ 4.35	1	L	C	×	
iv	A	12.50	+ 0.40	3	L	M		×
v	D	11.75	+ 2.05	2	D	D	×	×
vi	C	11.33	+ 0.23	-	L	L	×	×
vii	D	6.17	- 0.43	2	L	L		

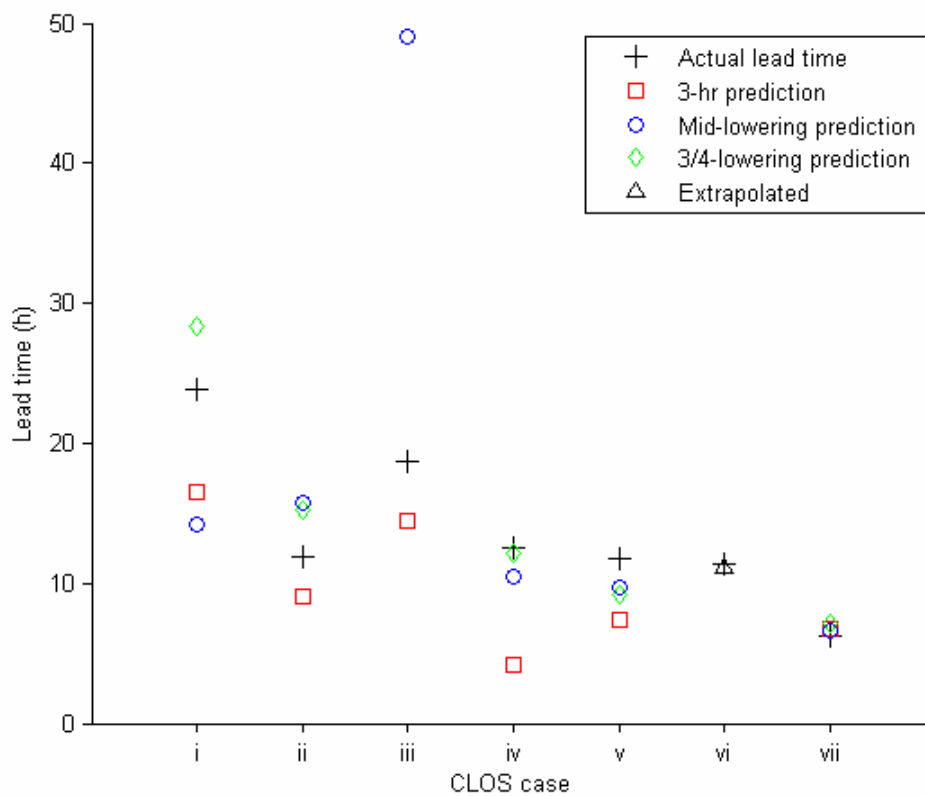


Figure 18. Nowcasting results for precipitation onset of the CLOS test cases using the developed decision tree.

As more cases are needed to fully test the DT and associated empirical and conceptual models, the results here are preliminary and cannot lead to any statistical rigor. However, three of the seven cases gave lead time predictions accurate within <1 hr of actual lead times up to 12.5 hr (Table 9). Furthermore, even CLOSs with actual lead times of nearly 24 hr (Case *i*) had a relatively low Nowcast error (< 5hr), with predictable subjective adjustments.

Case *iii* was not well handled by the models. When a lead time using Method 2 was calculated, an overall nowcast error of 30.35 hrs was produced. This can be attributed to the development of a lower-level cloud deck beginning at 21:00 (PDST) on February 10th (Figure 17c), which effectively attenuated the CLOS aloft, and thus proper interpolations of cloud-base heights for Methods 2 and 3 were not obtainable to run the lead time prediction models. Further investigation on handling lower-level cloud attenuation after CLOS onset is recommended.

Case *vi* (Figure 17f) was the most difficult case to nowcast. In fact, none of the derived regression models were applicable. Case *vi* was classified as a Class C synoptic map-type. The characteristic col of pressure was located directly over Vancouver (Figure 17f, left). Based on the “Subjective Predictors” for Class C, the CLOS was predicted to end in precipitation due to the location of the col onshore. Though no regression model was available to nowcast lead time Class C map-types, the CLOS maintained a linear lowering of cloud-base height (Figure 17f, left). Thus, only the initial cloud-base height was used in the predicted “Total Lowering” model. Visually extrapolating a linear fit from the initial cloud-base height to the predicted total lowering height along the observable cloud-base allowed for a nowcast lead time of 11.56 hr. The actual lead time was 11.33 hr, resulting in a nowcast error of +0.23 hr (~14 min). Considering the highly subjective extrapolation of lead time, Case *vi* was well predicted. Inferred from this is that models are not necessarily needed to nowcast the time of precipitation onset and signatures can be visually assessed when needed.

8.4 Assessment

Following the implementation of the developed forecasting approach and DT on the seven test cases, some distinct limitations and strengths inherent to the models are evident. The limitations are both caused by the empirical models, and the actual skill of the nowcaster. Using the current nowcasting approach, there is a marked trade-off between the time needed to produce the most accurate nowcast for precipitation onset, and the time that the nowcast is needed by the user, as further lowering of cloud-base (and thus longer time elapsed) resulted in the best lead time estimates. There are also significant limitations associated with lidar malfunctioning, whether it is due to down-time for maintenance, or significant CLOS attenuation by lower-level clouds (as in test Case *iii*). Moreover, some CLOSs may be missed entirely if they occur in periods of extended precipitation, when the lidar has not reactivated following the initial precipitation onset. The regression models were derived based on a relatively small dataset ($n = 75$), thus a larger dataset to both improve and test the models would provide better validation. Upscaling errors are probable, as the resulting lead time predictions effectively ‘contain’ the errors of the empirical models used (lead time and total lowering predicted). Finally, there is still some subjectivity involved for nowcasting the onset of precipitation (“Subjective Predictors”) which may or may not be able to be properly quantified in an automated detection and prediction system.

The strength of this method is that the data used to initialize the nowcasts are readily available to any user, specifically the lidar imagery and SLP maps. Unlike other nowcasting methods, the proposed conceptual model does not rely on dense local weather observations or even state of the atmosphere (Dabberdt 2002). Thus, the real-time use of the model is rather simplistic by nature, including the data which must be acquired to implement the models. Automated detection methods for cloud-base height already exist, which would allow the model to be automated with ease. Finally, by using the models in real-time, relatively accurate predictions were produced based solely on empirical and conceptual components. The previous section illustrated that nowcast errors are relatively low, especially when compared to the actual lead time to precipitation onset.

8.5 Future work and usage

As aforementioned, the DT model must be tested on more than the seven case studies. The advancement of the model will be lead by the overall skill scores and validation statistics produced by subsequent testing. As well, the possible site-specificity of the models should be investigated. The DT should be implemented in various similar locations and cities, or similar models with adjustments to the derived regression parameters should be done to test its overall applicability and accuracy.

More sophisticated data analyses should be conducted, especially concerning the basic meteorological data acquired from METARs. As discussed, these variables did not show any relationship to the overall RL, shape-type, or total lowering of the CLOSs. The lack of any relationships between variables is somewhat unexpected, and thus further steps should be taken in order to conclude if in fact the meteorological variables cannot be used as predictors in nowcasting from lidar imagery.

The influence of upper-air pressure fields (e.g. at the 800 mb level) were not investigated in this study. Further research could be undertaken to improve and refine the manual map classification scheme by coupling the classified SLP maps to their corresponding upper-level pressure maps. Currently, it is not known if the within-group variability of the map classes was caused by multi-level synoptic pressure fields. Moreover, a kinematic rather than static classification scheme should be investigated.

Forecasting and nowcasting products must be statistical, by nature. When the nowcasted lead time to precipitation onset is given in real-time, a statistical component must be provided to the users. For example, a useful statistical value would be reporting the likelihood that the actual lead time falls within the range of the predicted lead time. Again, these skill scores may be derived after repeatedly testing the models on more real-time CLOSs.

Nowcasting precipitation onset is useful to both the public and private sectors. Nowcasting methods vary widely and must be tailored to the user's needs (Dabberdt 2002). Workers in the tourism industry, construction, and even aviation safety could also benefit from higher quality nowcasts of precipitation onset. For example, during the Sydney (Australia) 2000 Olympics, nowcasting "precipitation onset time [was] important for event

organisers” (Keenan *et al.* 2003). Individuals of the general population, forecast modelers, hydrologists, and various private sectors may find the output of the lead time prediction models useful.

9.0 CONCLUSION

In this study, a phenomenological conceptual model for nowcasting precipitation onset in Vancouver was derived using CORALNet-UBC lidar imagery to determine cloud lowering signatures. By means of a manual synoptic map-typing scheme, followed by analysis of lidar-derived data and subjective examination, the Decision Tree model gave reasonable estimates of lead time to precipitation onset. However, these results were only preliminary due to the small dataset examined. Nevertheless, the real-time usage of lidar for active forecasting is possible, and may provide various public and private sectors with timely and accurate nowcasts. It is hoped that the results of this study may in fact serve as a precursor to automated methods that may exploit quantitative data as forecasting products.

REFERENCES CITED

- Anonymous.* (2009). Wind_rose. Available from MATLAB Central at <http://www.mathworks.com/matlabcentral/fileexchange/17748-windrose>
- Barry, R. G., Carleton, A. M. (2001). Synoptic and Dynamic Climatology. USA/Canada: Routledge
- Brooks, I. M. (2003). Finding boundary layer top: application of a wavelet covariance transform to lidar backscatter profiles. *Journal of Atmospheric and Oceanic Technology*, 20, 1092-1105
- Browning, K. A. (1980). Local weather forecast. *Proceedings of the Royal Society of London, Series A* , 371, 179-211
- Cadet, B., Giraud, V., Haeffelin, M., Keckhut, P., Rehou, A., Baldy, S. (2005) Improved retrievals of cirrus cloud optical properties using a combination of lidar methods. *Applied Optics*, 44, 1726–1734.
- Colman, B. (2003). “Challenges of forecasting in the West.” Nation Weather Service Warning Decision Training Branch, NOAA/National Weather Service [Conference]. Boulder, CO. Retrieved from *COMET Program, University Corporation for Atmospheric Research*. Retrieved from http://www.meted.ucar.edu/challenge_festwest/sectionmenu.htm
- Colquhoun, J. R. (1987). Forecast techniques: A decision tree method of forecasting thunderstorms, severe thunderstorms and tornadoes. *Weather and Forecasting*, 2, 337-345
- CORALNet. (2010). *The Canadian Operational Research Aerosol Lidar Network*, Retrieved from <http://www.coralnet.ca>
- Dabberdt, W. (2002). The scope and future of nowcasting. *Vaisala News*, 159, 33 - 37

- Environment Canada. (2010). Canadian Climate Normals 1971 – 2000. Retrieved October 15th, 2009, from http://www.climate.weatheroffice.ec.gc.ca/climate_normals
- Hogan, R. J., Illingworth, A. J., O'Connor, E. J., Poiares Baptista, J. P. V. (2003). Characteristics of mixed-phase clouds: Part II: A climatology from groundbased lidar. *Quarterly Journal of the Royal Meteorological Society*, 129, 2117–2134.
- Illingworth, A. J., Hogan, R. J., O'Connor E J Bouniol D Brooks M E Delanoë J Donovan D P Eastment J D Gaussiat N Goddard J W F Haeffelin M Klein Baltink H Krasnov O A Pelon J Piriou J.-M. Protat A. Russchenberg W J Seifert A Tompkins A M van Zadelhoff G.-J. Vinit F Willén U Wilson D R Wrench C L. (2007). CLOUDNET: Continuous evaluation of cloud profiles in seven operational models using ground-based observations. *Bulletin of the American Meteorological Society*, 88(6), 883-898
- Keenan, T. Joe, P, Wilson, J. Collier, C., Golding, B., Burgess, D. May, P., Pierce, C., Bally, J., Crook, A., Seed, A., Sills, D. Berry, L. Potts, R., Bell, I., Fox, N., Ebert, E., Eilts, M., O'Loughlin, K., Weeb, R., Carbone, R., Browning, K., Roberts, R., Mueller, C. (2003). Weather research program forecast demonstration project: Overview and current status. *American Meteorological Society*, 1041 – 1054.
- McKendry, I.G., van der Kamp, D., Strawbridge, K. B., Christen, A., Crawford, B. (2009). Simultaneous observations of boundary-layer aerosol layers with CL31 ceilometer and 1064/532 nm lidar. *Atmospheric Environment*, 43, 5847-5852
- Melfi, S.H.; Whiteman, D.; Rerrare, R. (1989). Observation of Atmospheric Fronts using Raman Lidar Moisture Measurements. *Journal of Applied Meteorology*, 28, 789-806
- Morille, Y. M., Haeffelin, M., Drobinski P., Pelon, J. (2007). STRAT: An automated algorithm to retrieve the structure of the atmosphere from single-channel lidar data. *Journal of Atmospheric and Oceanic Technology*, 24, 761-775

- Murayama, T., Sugimoto, N., Uno, I., Kinoshita, K., Aoki, K., Hagiwara, N., Liu, Z., Matsui, I., Sakai, T., Shibata, T., Arao, K., Sohn, B.-J., Won, J. G., Yoon, S. C., Li, T., Zhou, J., Hu, H., Abo, M., Iokibe, K., Koga, R., Iwasaka, Y. (2001). Ground-based network observation of Asian dust events of April 1998 in East Asia. *Journal of Geophysical Research*, 106(D16), 18345-18359
- Oke, T., Hay, J. (1994). *The Climate of Vancouver: 2nd Edition*. B.C Geographical Series, 50. Vancouver, Canada: Department of Geography, UBC
- Pal, S. R., Steinbrecht, W., Carswell, A. I. (1992). Automated method for lidar determination of cloud-base height and vertical extent. *Applied Optics*, 31(10), 1488-1494
- Pawlowicz, R. (2009). M_Map: A mapping package for MATLAB v1.4e. Available at <http://www.eos.ubc.ca/~rich/map.html>
- Rauthe, M., Gerding, M., Lübken, F. J. (2008). Seasonal changes in gravity wave activity measured by lidars at mid-latitudes. *Atmospheric Chemistry and Physics*, 8, 6775-6787.
- Steyn, D.G., Baldi, M., Hoff, R. M. (1999). The detection of mixed layer depth and entrainment zone thickness from lidar backscatter profiles. *Journal of Atmospheric and Oceanic Technology*, 16, 953-959
- Stull, R. (2009). *Meteorology for Scientists and Engineers: Draft for 3rd edition*. Canada: The University of British Columbia.
- The California Regional Weather Server. (2009). San Francisco State University, Meteorology Program, Department of Geosciences. Retrieved from <http://squall.sfsu.edu/crws.html>
- Unidata Program (2009). *The UCAR Community Programs*, University Corporation for Atmospheric Research.

van der Kamp, D., McKendry, I. G., Wong, M., Stull, R. (2008). Lidar ceilometer observations and modelling of a fireworks plume in Vancouver British Columbia. *Atmospheric Environment*, 42, 7174-7178

van Zadelhoff, G.-J., Donovan, D. P., Klein Baltink, H., Boers, R. (2004). Comparing ice cloud microphysical properties using CloudNET and Atmospheric Radiation Measurement Program data. *Journal of Geophysics Research*, 109, D24214, doi:10.1029/2004JD004967.

Wang, Z., Sassen, K. (2001). Cloud type and macrophysical property retrieval using multiple remote sensors. *Journal of Applied Meteorology*, 40, 1665-1682

Yarnal, B. (1993). Synoptic climatology in environmental analysis: A primer. London, United Kingdom: Belhaven Press

Yumimoto, K., Uno, I., Sugimoto, N., Shimizu, A., Liu, Z., Winker, D. M. (2007). Numerical modeling of Asian dust emission and transport with adjoint inversion using Lidar network observations. *Atmospheric Chemistry and Physics Discussions*, 7, 15955-15987

PLATE A: CATALOGUE OF CLOUD LOWERING SIGNATURES (CLOSs)

Case #	Season	Start time	End time	Shape type	Precip?	Start cloud-base (m)	End cloud-base(m)	Lead time (h)	Total lowering (m)	Rate of lowering (m/h)	Map Class
1	Sp	20/04/2008 04:00	21/04/2008 07:30	R	1	6800	600	27.50	6200	225.45	C
2	Sp	26/04/2008 12:00	27/04/2008 10:55	M	1	11300	1700	22.92	9600	418.91	A
3	Sp	04/05/2008 10:10	05/05/2008 07:00	M	1	9800	1700	20.83	8100	388.80	A
4	Sp	09/05/2008 14:25	10/05/2008 00:40	C	1	9800	1300	10.25	8500	829.27	A
5	Sp	12/05/2008 09:00	13/05/2008 02:25	L	1	9100	1800	17.42	7300	419.14	A
6	Sp	18/05/2008 13:30	19/05/2008 01:35	L	1	8600	2600	12.08	6000	496.55	F
7	Sp	25/05/2008 12:50	26/05/2008 00:20	L	1	5700	1400	11.50	4300	373.91	F
8	S	02/06/2008 15:00	02/06/2008 22:45	L	1	8200	1600	7.75	6600	851.61	A
9	S	18/06/2008 20:15	19/06/2008 09:50	L	1	9400	2000	13.58	7400	544.79	F
11	S	23/06/2008 04:30	24/06/2008 07:00	C	1	10300	1900	26.50	8400	316.98	B
12	S	25/06/2008 12:10	26/06/2008 10:50	M	1	6200	900	22.67	5300	233.82	A
13	S	25/07/2008 05:40	26/07/2008 10:55	L	1	11200	2400	29.25	8800	300.85	C
15	S	28/07/2008 04:10	29/07/2008 03:10	S	1	11500	2500	23.00	9000	391.30	A
16	S	30/07/2008 19:40	31/07/2008 08:45	L	1	5500	900	13.08	4600	351.59	B
18	S	19/08/2008 17:10	19/08/2008 19:30	D	1	6200	2700	2.33	3500	1500.00	A
19	S	21/08/2008 20:25	24/08/2008 5:50	R	1	10100	3400	57.42	6700	116.69	D
20	S	26/08/2008 10:15	26/08/2008 16:30	L	1	10000	1900	6.25	8100	1296.00	A
21	F	23/09/2008 5:30	23/09/2008 22:05	L	1	10000	1800	16.58	8200	494.47	B
22	F	26/09/2008 06:50	27/09/2008 10:20	L	0	7300	1500	27.50	5800	210.91	A
23	F	29/09/2008 18:45	02/10/2008 10:20	R	1	9200	1300	63.58	7900	124.25	E
26	F	15/10/2008 13:30	15/10/2008 19:35	L	1	4000	1200	6.08	2800	460.27	E
27	F	19/10/2008 08:35	20/10/2008 01:50	L	1	9400	2500	17.25	6900	400.00	A
28	F	21/10/2008 02:50	22/10/2008 23:55	R	1	9600	900	45.08	8700	192.98	B
29	F	23/10/2008 15:10	24/10/2008 15:05	C	1	10800	1700	23.92	9100	380.49	A
30	F	30/10/2008 06:20	30/10/2008 12:00	L	1	5800	2200	5.67	3600	635.29	B
31	F	03/11/2008 14:10	03/11/2008 21:30	L	1	2500	1200	7.33	1300	177.27	C
32	F	05/11/2008 04:05	05/11/2008 23:30	C	1	9000	800	19.42	8200	422.32	E
33	F	13/11/2008 14:50	14/11/2008 13:30	L	1	6100	1200	22.67	4900	216.18	B
35	F	19/11/2008 21:40	20/11/2008 09:20	S	1	10000	1800	11.67	8200	702.86	D
36	F	23/11/2008 04:30	25/11/2008 06:10	S	1	11100	1200	49.67	9900	199.33	B
37	F	26/11/2008 08:35	27/11/2008 10:50	R	1	5600	1400	26.25	4200	160.00	B
39	W	04/12/2008 13:30	05/12/2008 12:50		1	5400	1300	23.33	4100	175.71	H
43	W	29/12/2008 23:20	30/12/2008 06:10	C	1	2800	500	6.83	2300	336.59	E
44	W	08/01/2009 23:05	09/01/2009 08:50	R	1	8500	1200	9.75	7300	748.72	A
46	W	24/01/2009 03:15	25/01/2009 06:55	C	0	6300	1800	27.67	4500	162.65	C
47	W	26/01/2009 02:30	26/01/2009 23:10	S	1	8700	400	20.67	8300	401.61	B
48	W	28/01/2009 03:25	29/01/2009 02:35	L	1	8600	1200	23.17	7400	319.42	A
49	W	31/01/2009 17:50	01/02/2009 06:10	S	1	9800	700	12.33	9100	737.84	A
50	W	02/02/2009 19:50	05/02/2009 17:45	D	1	10400	1400	69.92	9000	128.72	D
51	W	07/02/2009 05:40	08/02/2009 19:45	S	1	9800	800	38.08	9000	236.32	A
52	W	09/02/2009 21:50	10/02/2009 05:40	D	1	7200	400	7.83	6800	868.09	D
53	W	13/02/2009 03:20	14/02/2009 22:15	C	0	7000	1000	42.92	6000	139.81	C
55	W	28/02/2009 08:20	28/02/2009 17:35	L	1	10200	800	9.25	9400	1016.22	B
56	Sp	05/03/2009 22:25	06/03/2009 23:15	N	1	10600	1000	24.83	9600	386.58	C
57	Sp	08/03/2009 03:50	09/03/2009 01:50	L	1	5500	600	22.00	4900	222.73	F
58	Sp	11/03/2009 15:10	13/03/2009 21:00	R	1	10600	1600	53.83	9000	167.18	B
59	Sp	20/03/2009 21:45	22/03/2009 21:45	L	1	7500	700	48.00	6800	141.67	D
60	Sp	25/03/2009 12:00	26/03/2009 23:30	C	1	8600	1500	35.50	7100	200.00	C
61	Sp	29/03/2009 17:50	30/03/2009 12:00	C	1	8800	1400	18.17	7400	407.34	A
62	Sp	31/03/2009 11:30	01/04/2009 05:55	D	1	7600	600	18.42	7000	380.09	B
63	Sp	07/04/2009 12:35	08/04/2009 20:25	C	1	11200	1000	31.83	10200	320.42	A
64	Sp	15/04/2009 18:20	16/04/2009 19:50	L	1	9000	1050	25.50	7950	311.76	A
65	Sp	17/04/2009 17:15	19/04/2009 00:45	L	1	6400	1200	31.50	5200	165.08	D
66	Sp	21/04/2009 06:30	21/04/2009 19:20	S	1	9400	1900	12.83	7500	584.42	D
67	Sp	24/04/2009 08:00	25/04/2009 07:20	L	0	9200	500	23.33	8700	372.86	F
68	Sp	26/04/2009 02:10	29/04/2009 09:20	R	0	11600	2500	79.17	9100	114.95	F
69	Sp	01/05/2009 09:20	02/05/2009 11:05		1	9600	1800	25.75	7800	302.91	G
72	Sp	14/05/2009 20:20	18/05/2009 11:45	M	1	10500	1400	87.42	9100	104.10	B
73	Sp	20/05/2009 15:45	21/05/2009 04:15	L	0	7400	3900	12.50	3500	280.00	F
74	Sp	24/05/2009 06:10	25/05/2009 22:30	R	1	10400	2200	40.33	8200	203.31	A
75	Sp	31/05/2009 09:30	02/06/2009 10:20	R	0	10200	5700	48.83	4500	92.15	F
76	S	10/06/2009 11:40	10/06/2009 22:35	D	0	11000	2200	10.92	8800	806.11	B
77	S	11/06/2009 17:40	11/06/2009 22:35	L	0	10600	6200	4.92	4400	894.92	F
78	S	15/06/2009 22:00	16/06/2009 19:05	L	1	11400	2400	21.08	9000	426.88	A
79	S	20/06/2009 00:30	21/06/2009 19:35	L	1	9400	2200	43.08	7200	167.12	F
80	S	22/06/2009 20:00	23/06/2009 20:05	S	1	11100	2200	24.08	8900	369.55	A
81	S	26/06/2009 22:05	27/06/2009 17:35	S	1	11100	1400	19.50	9700	497.44	A
82	S	03/07/2009 23:35	06/07/2009 06:05	L	1	11000	400	54.50	10600	194.50	C
83	S	20/07/2009 08:20	20/07/2009 19:25	L	0	10600	7900	11.08	2700	243.61	F
84	S	23/07/2009 06:35	24/07/2009 12:15	C	0	7700	1100	29.67	6600	222.47	A
88	S	16/08/2009 14:10	17/08/2009 12:55	M	0	11900	5800	22.75	6100	268.13	F
89	S	24/08/2009 01:55	25/08/2009 01:45	L	1	12200	3000	23.83	9200	386.01	B
90	S	25/08/2009 21:55	28/08/2009 21:55	R	1	11000	6600	72.00	8000	111.11	B
92	F	11/10/2009 00:00	12/10/2009 23:50		1	8800	800	47.83	8000	167.25	H
93	W	05/01/2010 12:40	07/01/2010 18:25		1	8800	1700	53.75	7100	132.09	G